JGR Solid Earth

RESEARCH ARTICLE

10.1029/2020JB020350

Key Points:

- We describe a method for inverting multifrequency Ps and Sp receiver functions for mantle thermochemical structure
- We distinguish tectonic regions based on thermochemical characteristics across the United States from the active West to the cratonic-orogenic East
- We observe strong thermochemically induced and interrelated topographic variations of the lithospheric base and the 410-km discontinuity

Supporting Information:

- Supporting Information S1

Correspondence to:
F. Bissig,
felix.bissig@erdw.ethz.ch

Citation:
Bissig, F., Khan, A., Tauzin, B., Sossi, P. A., Munch, F. D., & Giardini, D. (2021). Multifrequency inversion of Ps and Sp receiver functions: Methodology and application to USArray data. *Journal of Geophysical Research: Solid Earth*, *126*, e2020JB020350. https://doi.org/10.1029/2020JB020350

Received 5 JUN 2020
Accepted 11 NOV 2020
Accepted article online 18 NOV 2020

Multifrequency Inversion of Ps and Sp Receiver Functions: Methodology and Application to USArray Data

Felix Bissig[1], Amir Khan[1,2], Benoit Tauzin[3,4], Paolo A. Sossi[5], Federico D. Munch[6], and Domenico Giardini[1]

[1]Institute of Geophysics, ETHZ, Zürich, Switzerland, [2]Institute of Theoretical Physics, University of Zürich, Zürich, Switzerland, [3]Research School of Earth Sciences, ANU, Canberra, Australia, [4]Université de Lyon, Université Claude Bernard Lyon 1, ENS, CNRS, Laboratoire de Géologie de Lyon: Terre, Planètes, Environnement, Villeurbanne, France, [5]Institute of Geochemistry and Petrology, ETHZ, Zürich, Switzerland, [6]Department of Earth and Planetary Science, University of California, Berkeley, CA, USA

Abstract We image the thermochemical structure of crust and mantle underneath the North American continent by inverting recordings of P-to-s (Ps) and S-to-p (Sp) converted seismic body waves (receiver functions [RFs]). Through careful data selection and processing, we construct a multifrequency Ps (5-, 8-, and 10 -s) and Sp (10- and 15- s) RF data set from USArray recordings. The inversion is interfaced with petrological phase equilibria computations to build self-consistent radial seismic velocity and density models for RF waveform simulations. Inverted models are combined through back-projection along converted raypaths and interpolation to tomographic images of crust and mantle structure. Through clustering analysis we identify three major tectonic regions based on mantle thermochemical and seismic structure: the tectonically active West (TAW), the central transition region (CTR), and the cratonic-orogenic East (COE). TAW is chemically more fertile with a Mg# ~ 0.90 (molar Mg# $=$ Mg/(Mg $+$ Fe)) and characterized by an elevated mantle potential temperature of 1490 ± 27°C relative to COE, which is chemically more depleted (Mg# ~ 0.91) and colder (1419 ± 27°C). CTR is intermediate to TAW and COE. We find significant thermochemically induced topography associated with the base of the lithosphere (± 90 km), while the mantle transition zone is mostly influenced by thermally induced topography on the 410-km discontinuity (± 15 km). In contrast, the 660-km discontinuity, where variations are only ± 5 km, reflects a more complex thermochemical interplay. To place the results in a tectonic context, thermobarometric estimates from basaltic rocks across the western United States are integrated with the seismic inversions to produce a thermal model of the underlying mantle.

1. Introduction

Earth's thermal and compositional structure is the result of wide-ranging dynamical processes that have shaped and continue to shape the planet's surface and interior. Seismology provides tools for imaging traces of these processes, such as subducting slabs, thick continental roots, and mantle plumes, through their influence on material properties and thus seismic wave velocities and propagation.

The aforementioned geologic features can be seismically imaged using converted, reflected, and refracted body waves (e.g., Farra & Vinnik, 2000; Flanagan & Shearer, 1998; Tan & Helmberger, 2007). For example, the construction of receiver functions (RFs) allows to extract timing and amplitude of P-to-s (Ps) and S-to-p (Sp) converted phases, which serve as proxy for imaging depth and sharpness of seismic discontinuities beneath a station, respectively (Langston, 1979; Vinnik, 1977). Important seismic discontinuities include the base of the crust (Moho), the lithosphere-asthenosphere boundary (LAB), and the bounding discontinuities of the mantle transition zone (MTZ; cf. Figure 1).

While the LAB primarily marks a change in thermal and rheological regime (e.g., Artemieva & Mooney, 2001; Eaton et al., 2009; Jaupart & Mareschal, 1999), two globally observable discontinuities bound the MTZ that are associated with the transformation of the mantle minerals olivine to wadsleyite and ringwoodite to bridgemanite + ferropericlase at depths of ∼410- and ∼660-km depth, respectively (Dziewonski & Anderson 1981; Ringwood, 1975). The exact depth of these discontinuities (hereafter referred to as 410

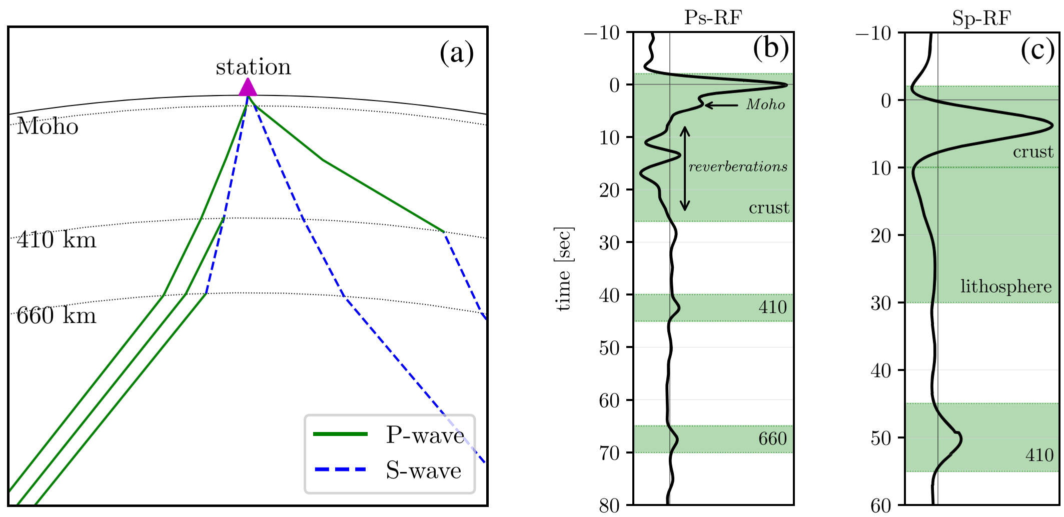

Figure 1. Illustration of conversions of body waves at (a) the Moho and the 410- and 660-km seismic discontinuities in the Earth and corresponding synthetic (b) Ps and (c) Sp receiver functions based on the seismic reference model IASP91 (Kennett & Engdahl, 1991). *P* and *S* waves are shown as green (solid) and blue (dashed) lines, respectively. Time windows including arrivals of converted waves are shaded in green. Note that the polarity and time axis of Sp RFs are flipped as a result of which arrivals with positive travel times arrive prior to the *S* wave and are not masked by crustal reverberations as is the case for Ps conversions.

and 660) is a nonlinear function of local temperature, pressure, and composition (Bina & Helffrich, 1994; Helffrich, 2000; Xu et al., 2008). The RF technique serves as an excellent tool to study lateral thermochemically induced variations in discontinuity structure (e.g., Andrews & Deuss, 2008; Cottaar & Deuss, 2016; Geissler et al., 2010; Kumar et al., 2005; Knapmeyer-Endrun et al., 2017; Lawrence & Shearer, 2006; Makushkina et al., 2019; Monna et al., 2019; Munch et al., 2020; Sodoudi et al., 2006; Tauzin et al., 2008, 2017; Vinnik, 2010).

Here, we consider Ps and Sp RFs to study crust, lithosphere, and mantle underneath the contiguous United States, which offers a plethora of past and recent geologic processes and encompasses areas from active tectonic regions in the west to precambrian and phanerozoic continental masses in the central and eastern parts (cf. Figures 2a and 2b; Hoffman, 1989; Mooney & Kaban, 2010; Williams et al., 1991; Whitmeyer & Karlstrom, 2007). Extensive seismic studies of the North American lithosphere, its base, and intralithospheric discontinuities have been conducted and provided insights into the processes that formed these complex continental entities (e.g., Abt et al., 2010; Afonso et al., 2016; Boyce et al., 2019; Calò et al., 2016; Eilon et al., 2018; S. M. Hansen et al., 2015; Kind et al., 2015, 2020; Rychert et al., 2007; H. Yuan & Romanovicz, 2010; H. Yuan et al., 2014). Seismic imaging of the mantle have tracked both recent (e.g., Juan de Fuca slab and Yellowstone plume) and ancient tectonic features (e.g., Farallon slab) (e.g., Burdick et al., 2008; C. Chen et al., 2015; Krischer et al., 2018; Maguire et al., 2018; Nelson & Grand, 2018; Nettles & Dziewonski, 2008; Obrebski et al., 2010; Porritt et al., 2014; Sigloch, 2011; van der Lee & Nolet, 1997).

In this study, we aim to improve our current understanding of mantle structure and its relation to past and present dynamical processes underneath the North American continent by providing a more detailed view of the combined thermochemical structure of Moho, LAB, upper mantle, and MTZ. For this purpose, we will build upon and extend the work of Munch et al. (2018), who combined mineral phase equilibrium computations with geophysical inversion to self-consistently image the thermochemical structure of the MTZ using Ps waves converted at the 410 (P410s) and 660 (P660s). The advantage of this approach is that it anchors temperature, composition, seismic properties, and discontinuities that are in laboratory-based forward models, while simultaneously permitting, through inversion, to optimize profiles of physical properties (e.g., *S* wave velocity) to match seismic data.

We consider a number of improvements and extensions to our previous work by (1) including Sp RFs; (2) considering multiple frequency bands for both Ps and Sp RFs; and (3) applying the methodology to USArray data to perform a tomographic study of the North American continent. Points 1 and 2 allow for improvement

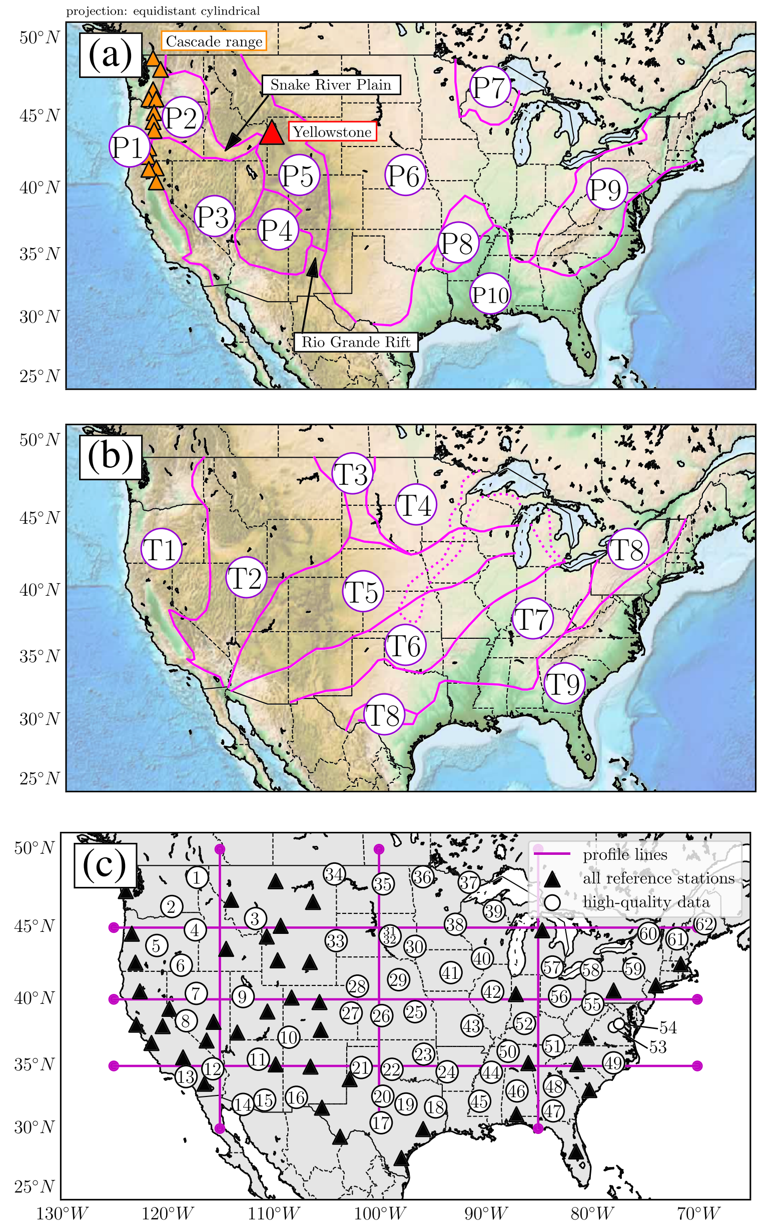

Figure 2. (a) Main physiographic features (Fenneman, 1928) of the contiguous United States: P1: Pacific mountain system (including Cascade Range); P2: Columbia plateau (including Snake River Plain and Yellowstone Hotspot); P3: Basin and Range (including Rio Grande Rift); P4: Colorado plateau; P5: Rocky Mountain system; P6: Interior Highlands; P7: Laurentian Highlands; P8: Interior Highlands; P9: Appalachian Highlands; P10: Atlantic Plain. (b) The tectonic provinces (Hoffman, 1988; Whitmeyer & Karlstrom, 2007) represent the long-term geological history of the continent: the oldest parts of the continent, i.e., of Precambrian age, include the Greater Wyoming province (T2) and Superior craton (T4), which are connected along the Trans-Hudson orogen (T3). Proterozoic orogenies accreted the Yavapai (T5), Mazatzal (T6), Granite-Rhyolite (T7), and Grenville provinces (T8) to the cratonic core. During episodes of extension in proterozoic times, the mid-continental rift was formed but abandoned, and later, the Pacific and paleo-Atlantic oceans were opened. The closure of the latter during the paleozoic formed the Appalachian mountain belt (T9 and P9), which, nowadays, is bordered by the Atlantic plains (P10), i.e., the relatively young passive continental margin, to the east and south. In contrast to the east, the western margin (T1) is dominated by subduction processes acting since the mesozoic (e.g., Dickinson, 2004; Humphreys, 2009; Sonder & Jones, 1999), which have resulted in accretion of terrane to the American continent, volcanism (Cascade range, P1), and extensional tectonics (Basin and Range, P3). The topography model underlying the maps is that of ETOPO1 (Amante & Eakins, 2009). (c) Location of USArray reference stations (www.usarray.org). White circles indicate stations, where either Ps or Sp RFs or both were inverted, while black triangles represent stations for which data were processed but because of quality constraints were not considered in the inversion. Station numbering and details are given in Table S1. Magenta lines indicate profiles along which cross sections of mantle seismic properties are shown.

in resolution of lithosphere, upper mantle, and MTZ structure. With these improvements in place, we are able to identify three major tectonic provinces based directly on differences in mantle thermochemical and seismic structure that show significant thermochemically induced variations across the LAB and MTZ. We further observe well-known tectonic features in our tomographic images, such as hot mantle upwelling underneath the western United States as well as traces of active and ancient subduction.

This paper is divided into two parts: a methodological and an application part. In part 1 (sections 2 and 3), we describe how seismic data are processed to construct a new set of multifrequency Ps and Sp RFs using USArray data with particular emphasis on Sp RFs (Ps RFs are detailed in Munch et al., 2018), including data selection, deconvolution, spatial sensitivity analysis, stacking and uncertainty estimation, and RF modeling as part of which we perform a benchmark of one-dimensional (1-D) synthetic waveforms against three dimensional (3-D) full waveform synthetics to validate our 1-D modeling approach to computing seismograms. In part 2 (sections 4–7), we apply the developed methodology to obtain self-consistent tomographic images of the crust, lithosphere, and mantle underneath the North American continent. Part 2 includes model parametrization, inversion procedure, and discussion of results. Finally, to further test the results presented here, we compare our seismic thermal model with an independent model of the western United States constructed from thermobarometry data.

2. Data Processing

The fundamental idea of the RF method is to separate signals generated by the direct and converted phases on three-component ground-motion recordings based on their distinct particle motion (e.g., Kind et al., 2012; Rondenay, 2009). In the case of a Ps conversion, the P motion is recorded on the vertical component and the converted wave on the radial component, while the order is reversed for Sp conversions. The converted signal can be considered as the convolution of the direct wavefield with the local structural response. Thus, deconvolving the "source" (i.e., direct phase) from the "response" trace (i.e., converted phase) results in a time series representing the structure below the receiver (Langston, 1979; Vinnik, 1977). This time series is called the receiver function (cf. Figures 1b and 1c). Source and path effects between event and conversion point are assumed to be removed through the deconvolution operation, as all this information is contained in both, source and response traces (Kind et al., 2012).

In spite of certain advantages of Sp over Ps RFs, the use of the former for making structural inferences is limited relative to the latter because of limitations that beset *S* waves (e.g., Bock, 1994; Farra & Vinnik, 2000; Wilson et al., 2006; X. Yuan et al., 2006). First, the incidence angle of Sp converted phases is larger than that of the original *S* wave, causing post-critical incidence to restrict the usage of Sp RFs to narrower epicentral distance ranges and depths shallower than 660 km (cf. Figure 1a). Also, because of the large incidence angle, Sp conversion points are located farther away from the station than in the case of Ps, which ultimately results in broader regional sampling. Added to this is a lower spatial resolution because of a lower frequency content of *S* waves relative to *P* waves. Second, the signal-to-noise ratio (SNR) of *S* waves is lower than for *P* waves because of a range of interfering phases, which generally complicates observation of Sp conversions. In this context, Bock (1994) and Wilson et al. (2006) have pointed out that amplitudes of *P* wave multiples between the surface and the MTZ can become significant to the extent that these can be mistaken for conversions. Third, core phases (ScS, SKS, and their respective conversions) in the epicentral distance range ~85° to 100° interfere with Sp conversions, in particular the S660p phase (X. Yuan et al., 2006). These issues can, however, to a large extent be mitigated through careful data selection and processing steps as described in, for example, Monna et al. (2019); X. Shen et al. (2019); and Wilson et al. (2006).

2.1. Data Selection

We collected and processed data recorded at stations of the USArray (Figure 2c), which includes about 100 reference stations in complementary use to the denser transportable network. Seismic data were acquired from the IRIS datacenter (Incorporated Research Institutions for Seismology, ds.iris.edu/ds/nodes/dmc/) using ObspyDMT (Hosseini & Sigloch, 2017). Event selection is based on information available from the global centroid moment tensor catalogue (www.globalcmt.org, Dziewonski et al., 1981; Ekström et al., 2012). Only events with a magnitude of at least 5.5 and a focal depth shallower than 150 km were selected. The latter criterion is applied to reduce the interference of Sp conversions with surface-reflected multiples (Wilson et al., 2006). For constructing Ps RFs, we select events in the epicentral distance (Δ) range of 40° to 95° (e.g., Andrews & Deuss, 2008). For Sp RFs, we are restricted to a Δ range of 55° to 90° because of post-critical incidence. Also, because of the simultaneous arrival of SKS and ScS (including their conversions) beyond 85°, the S660p conversion is very difficult to observe (X. Yuan et al., 2006). We therefore focus on Sp conversions at discontinuities between the Moho and the 410. The selected distance ranges and the respective travel times of direct and converted waves are shown in Figure S1 in the supporting information.

2.2. RF Processing

For each event, recordings are filtered between 0.02 and 1 Hz using a Butterworth bandpass filter of second order and are then rotated to the vertical-radial-transverse (ZRT) system under consideration of the back-azimuth computed from the source and receiver locations. In the Sp case, we additionally rotate waveforms to the LQT system, where the orthogonal L and Q components are approximately aligned with the S and Sp converted phases, respectively, improving their detectability (Kind et al., 2012; Rondenay, 2009). The orientation of the L and Q axes is determined by maximizing the energy in the window from −30 to +50 s on the Z/L component around the theoretical S-wave arrival by means of principal component analysis (PCA; see Figure S2). In order to determine the SNR and exact arrival of the direct phase, we implemented the automated picking approach of Abt et al. (2010). An illustration hereof is shown in Figure S3. To ensure high-quality data, we only consider waveforms with a SNR > 5. Alternative SNR criteria for detecting lithospheric Sp conversions have also been proposed by X. Shen et al. (2019) and Monna et al. (2019).

2.2.1. Deconvolution

RFs are obtained from deconvolving source (direct phase) from response waveform (converted phase). The source wavelet is extracted by trimming the corresponding trace around the picked arrival of the direct phase within windows from −50 to +150 s and from −100 to +30 s for Ps and Sp RFs, respectively. Analogously, the response trace is cut within a window from −50 to +150 s and from −150 to +50 s for Ps and Sp RFs, respectively. The tapered source and response waveforms are subsequently deconvolved using iterative time-domain deconvolution (Ligorría & Ammon, 1999). For removing high-frequency noise from the RFs, a Butterworth low-pass filter of second order is applied for different corner periods: 5-, 8-, and 10- s for Ps RFs and 10- and 15- s for Sp RFs. This choice is dictated by the increased noise content at shorter periods and lack of resolution at longer periods, respectively. Maximum wavelengths associated with these periods are 28–56 km for Ps and 90–135 km for Sp RFs, respectively. Since the arrival times of converted phases not only depend on the structure below the receiver but also on the slowness of the ray, we stretch and compress the time axis of each RF to a reference slowness (moveout correction), i.e., 6.5 s/° for Ps RFs and 9.9 s/° for Sp RFs. For comparison with Ps RFs, the time axis and polarity of Sp RFs are flipped.

2.2.2. Stacking and Uncertainty Estimate

To further enhance SNR, we stack individual RF traces at a given station. This ensures that information from many events, where focal depth, mechanism, and epicentral distance differ, are combined coherently. Phases not aligned through the moveout correction are canceled and hence direct conversions enhanced. To determine uncertainties on RFs, we employ a bootstrap resampling approach (Efron & Tibshirani, 1991) and compute the standard deviation of 100 stacks, where each stack is formed from n randomly recombined RFs, with n being the number of available RF traces. A crucial choice has to be made on the selection of RF traces to be included in a stack, as this depends on the spatial sensitivity of the data set, i.e., location of conversion points relative to station and frequency content.

2.2.3. Spatial Sensitivity of Sp RFs

Assuming the main sensitivity of a RF to be confined to the region directly beneath the station allows us to sum all moveout-corrected RF traces available to form a stack. While this assumption is reasonable for Ps conversions and therefore applied to the Ps RF data set, it is not directly applicable to the Sp conversions, because of the high incidence angles compared to the direct S wave. Consequently, Sp conversion points are located significantly further away from the station than those of Ps converted waves from the same depth (cf. Figure 1a). Moreover, Sp converted waves propagate faster and hence have longer wavelengths. These effects are illustrated for Sp RFs obtained at station 39-COWI ("39" referring to the station ID in Figure 2c and "COWI" being the station abbreviation) and filtered at 10s period by computing and plotting the Fresnel volumes of converted waves at different depth slices following the approaches of Lekić et al. (2011) and Cottaar and Deuss (2016). For each event present in the Sp RF data set for station 39-COWI, we (1) determine Sp conversion points at depth Z using ray tracing through IASP91 (Crotwell et al., 1999;

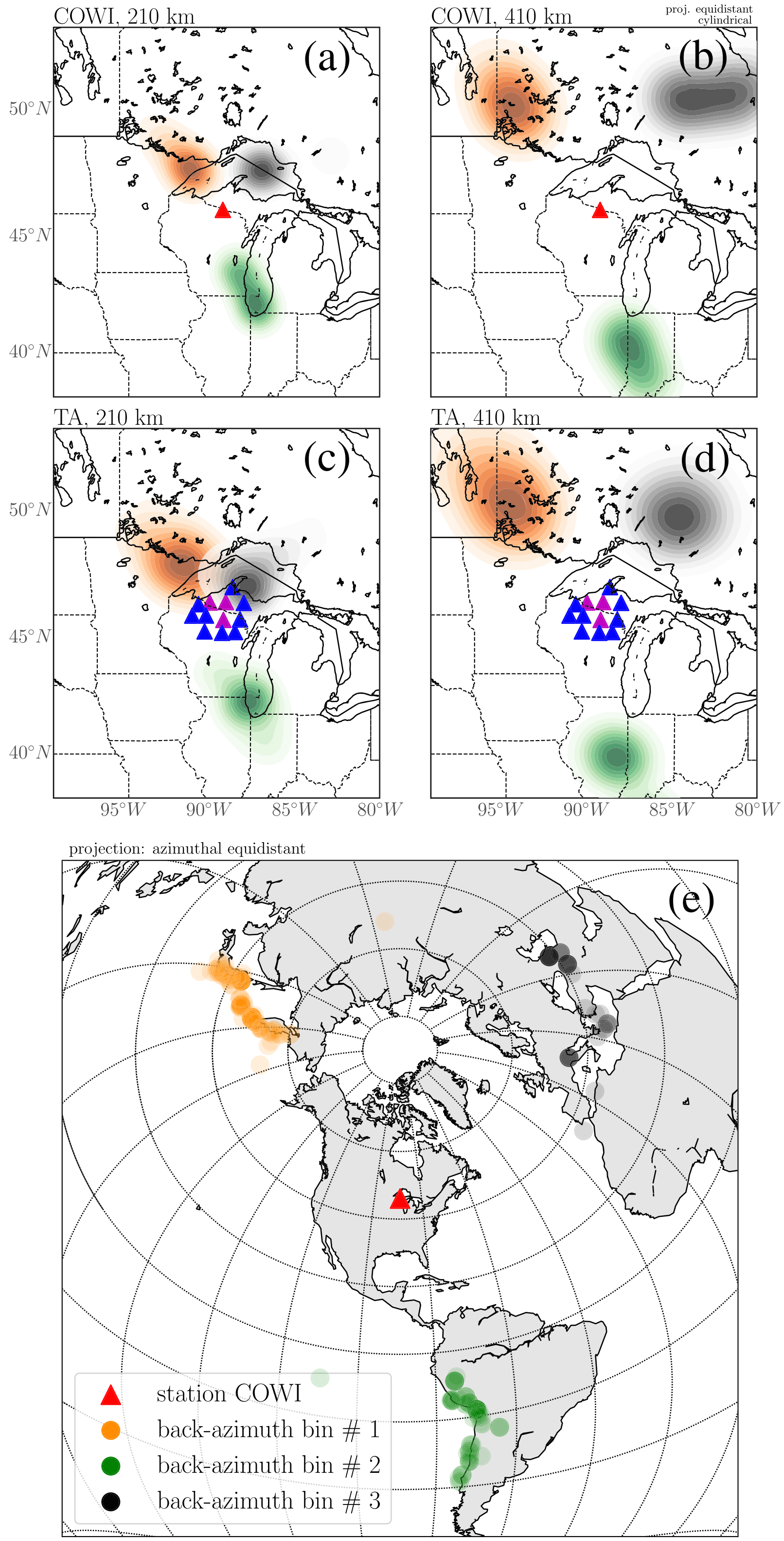

Figure 3. (a–d) Normalized Fresnel zone weights of Sp piercing points (color coded by back-azimuth; see panel e) at a depth of 210- (a and c) and 410- km (b and d) for the events recorded at 39-COWI (red triangle) and 12 nearby transportable USArray stations within a distance of ~70- (TA1; magenta triangles) and ~140- km (TA2; blue triangles), respectively. (e) Location of station 39-COWI and the seismic events used for computing Sp receiver functions colored by back-azimuth (dots).

Kennett & Engdahl, 1991) and (2) compute the Fresnel zone half-width, δ^{HW}, at the same depth Z, which is a function of wavelength, λ, via

$$\delta^{HW} = \sqrt{\left(\frac{\lambda}{3} + Z\right)^2 - Z^2}, \tag{1}$$

where λ is obtained by multiplying the P wave velocity above Z, i.e., the velocity of the converted wave, with the dominant period (here 10 s). Knowing the location of conversion points and Fresnel zones, we evaluate the lateral sensitivity of the ray by comparing δ^{HW} for each node on a discrete grid at distance δ to the conversion point of interest via normalized cubic splines:

$$\mathrm{w} = \begin{cases} \frac{3}{4}\bar{\delta}^3 - \frac{3}{2}\bar{\delta}^2 + 1, & \text{if} \, \bar{\delta} \leq 1 \\ \frac{1}{4}(2-\bar{\delta})^3, & \text{if} \, 1 < \bar{\delta} \leq 2 \\ 0, & \text{if} \, \bar{\delta} \geq 2, \end{cases} \tag{2}$$

where $\bar{\delta} = \delta/\delta^{HW}$. We performed this analysis for conversions at 210- and 410-km depth (see Figures 3a and 3b). The weights of all rays included in a certain back-azimuth bin are summed and rescaled by the maximum value to facilitate comparison. Note that the width of the Fresnel volume is not the resolution limit of a seismic wave (Spetzler & Snieder, 2004) but serves as a useful illustration of the latter.

For station 39-COWI, we observe that the group of events emanating from the western Pacific, South America, and Europe (Figure 3e) produce distinct sensitivity clusters at 210- and 410-km depth (Figures 3a and 3b). Their clear separation indicates that summing RFs from the entire data set would lead to averaging of lithospheric and upper mantle structure from different regions. Instead, it requires forming stacks that are sorted by back-azimuth (e.g., Monna et al., 2019; Vinnik, 2005, 2010). However, back-azimuth binned stacks reduce the number of useful traces available in one back-azimuth bin to between 10 and 80; yet Sp RF stacks containing less than ~100 traces tend to be noisy and, consequently, less robust (see section S2). A possible work-around is to increase the number of traces within a back-azimuth bin by incorporating additional data as shown in the following.

2.2.4. Back-Azimuth Stacking Using Additional Stations

In addition to the reference network (Figure 2c), USArray also consists of a dense network of transportable stations. Since stations are only spaced about 60 km apart, events of similar back-azimuth recorded at neighboring stations will produce Sp converted waves that sample a similar region as illustrated in Figures 3c and 3d. Thus, the amount of data in a back-azimuth bin for a given reference station can be increased by including data recorded at nearby transportable stations.

This is illustrated in Figure 4 for the reference station 39-COWI, which shows how the uncertainty and amplitudes of the Sp RF stack evolve as traces from the transportable stations closest to 39-COWI are added for events in the western Pacific (back-azimuth bin #1, panels a and b) and Europe (back-azimuth bin #3, panels c and d), respectively. For both back-azimuth clusters, we see that the bootstrap-derived mean uncertainty of the cumulative stack decreases and that RF amplitudes change when the number of traces is increased. The improvement in the quality of the Sp RF is particularly evident in the case of the S410p phase that emerges in back-azimuth bin #3, which is far less apparent in the Sp RF 39-COWI-only stack. Although the final number of traces used (~50) for this particular event cluster remains below the threshold associated with a robust stack, back-azimuth bin #1 includes more than 150 traces. In combination with the clear signals emanating from Moho, lithosphere, and the 410, we therefore consider this to be a high-quality stack and retain it for the inversion.

An alternative approach would be common-conversion point (CCP) stacking, which migrates each individual RF trace from time to depth domain according to its conversion points (e.g., Cottaar & Deuss, 2016; Dueker & Sheehan, 1997; Kosarev et al., 1999; Kind et al., 2020; Lekić & Fischer, 2014; Lekić et al., 2011; Lekić & Fischer, 2017; Rondenay, 2009). This method, however, depends crucially on the background velocity model used for migration and, unless data are properly reprocessed during inversion using the currently updated velocity model, is not self-consistent and therefore limited in accuracy.

2.3. Data Workflow Summary

We processed Ps and Sp RFs for all USArray reference stations (Figure 2c). This included the following steps:

10.1029/2020JB020350

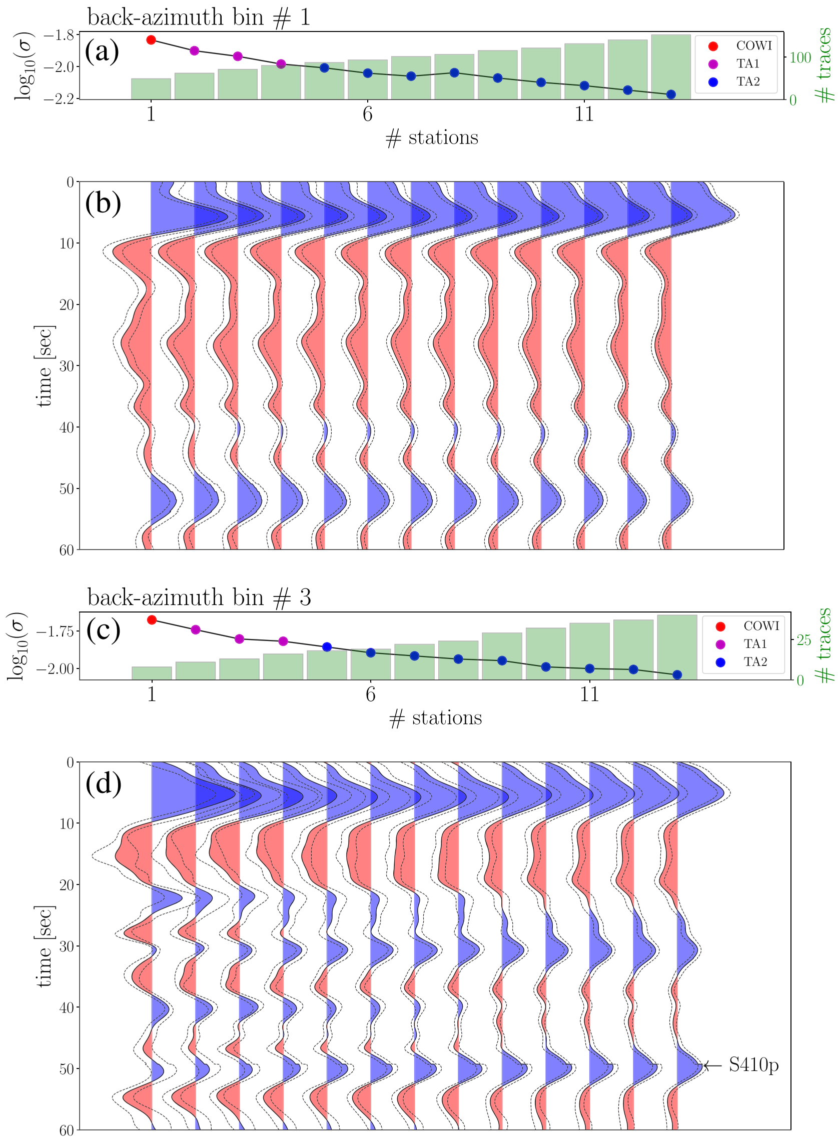

Figure 4. Sp receiver function stacks, mean uncertainty (σ), and number of summed traces (green bars) for two distinct back-azimuth bins related to events in the (a and b) west Pacific (#1) and (c and d) Europe (#3), respectively. Including data recorded at transportable stations (blue and magenta dots; TA1 and TA2, respectively) of the reference station (39-COWI; red dot) reduces uncertainty and enhances the S410p phase in back-azimuth bin #3 (d).

- Construction of a multifrequency Ps (5-, 8-, and 10-s low-pass period) and Sp (10- and 15-s low-pass period) RF data set.
- Formation of Sp RF stacks sorted by back-azimuth by combining data recorded at USArray reference and transportable stations that are located at a maximum distance of 140 km from the former.
- Selection of robust and only highest quality Ps and Sp RFs with clear signals emanating from the Moho, lithosphere, 410, and 660 for the inversion (cf. Table S1).

3. Synthetic RF Modeling

In order to generate a synthetic RF stack equivalent of the observed RF stack, we first compute waveforms using the reflectivity method (Fuchs & Müller, 1971; Müller, 1985). In order to ensure consistency, synthetic waveforms are processed the same way as the observed data (Munch et al., 2018). For optimal radiation of *P* and *SV* waves, we model the source as an explosion for Ps RFs and a normal-fault mechanism for Sp RFs. The source-time function is a Heaviside function and the modeled focal depth is imposed by the median of the depth distribution of the observed events. As the amplitudes of converted waves depend on slowness, their relative contribution to the final RF stack has to be mimicked in the synthetic RF modeling. The distribution of receivers and their relative weights in the stack therefore follows that of the distribution of the theoretical slownesses of the direct phase as imposed by the data set (Munch et al., 2018).

We exclude the uppermost layer of the model from the reflecting zone when computing waveforms for Sp RFs (cf. Figure S6). This suppresses multiple surface reflections which otherwise would constructively interfere and bias the RF. This approach is similar to the one by X. Yuan et al. (2006), who argue that propagation of multiples in a laterally heterogeneous Earth is ineffective. Ultimately, synthetic waveforms also have to conform to the following criteria: (1) the L and Q axes as imposed by the data set are employed to ensure consistency between observed and synthetic LQT-systems, since these affect RF amplitudes, and (2) the arrival time of the direct phase for the underlying model is determined via ray tracing (Crotwell et al., 1999), since the automated picking algorithm is unable to distinguish core phases from S waves for $\Delta > 85°$.

Finally, in order to validate our 1-D modeling approach to computing synthetic seismograms, we benchmarked modeled 1-D RFs against 3-D full waveform synthetics (see section S3.2). For this purpose, we employed the spectral element based software package Salvus (Afanasiev et al., 2019) to compute full waveforms in a 3-D velocity model. Comparison of 1-D and 3-D RFs is shown in Figure S7 and the modeled waveforms are seen to be in good agreement. On the basis of this benchmark, the 1-D approach pursued here appears to be reliable for modeling both, Ps and Sp RFs, and, from a practical viewpoint, computationally much more efficient (1-D: ∼15–20 s on a normal desktop-computer per RF stack, 3-D: ∼25 nodehours on a supercomputer).

4. Model Parametrization

4.1. Petrological Model

Building on previous experience (e.g., Khan et al., 2009; Munch et al., 2018), we model mantle composition by the weight fraction of basalt in a basalt-harzburgite mixture. This compositional model is based on the recognition that basaltic crust is generated at ridges through partial melting, leaving behind the depleted complement harzburgite (Xu et al., 2008). At subduction zones, this physically and chemically stratified oceanic lithosphere is continuously being recycled back into the mantle, where it remixes (e.g., Helffrich & Wood, 2001; Tackley et al., 2005). The resultant mineralogy depends on the degree of equilibration between basalt and harzburgite and two mixing models have been proposed (Xu et al., 2008): equilibrium assemblage (EA) and mechanical mixture (MM). The EA model assumes full equilibration, whereas in the MM model the mantle is a mixture of the end-members. Here, we focus on the EA model as Munch et al. (2018) have shown that RFs are less sensitive to differences between MM and EA.

For a given basalt fraction f, mantle composition $\mathbf{X}$ is computed from

$$\mathbf{X} = f\mathbf{X}_B + (1 - f)\mathbf{X}_H, \tag{3}$$

where $\mathbf{X}_B$ and $\mathbf{X}_H$ are basaltic and harzburgitic end-member compositions, respectively. To predict the relative amount of stable minerals and physical properties along a self-consistent mantle adiabat for harzburgite and mid-ocean ridge basalt (MORB) chemical compositions in the Na_2O-CaO-FeO-MgO-Al_2O_3-SiO_2 system (Table 1), we employ Gibbs free energy minimization and equation-of-state modeling (Perple_X software package; Connolly, 2009). For this purpose, we adopt the thermodynamic formulation of Stixrude and Lithgow-Bertelloni (2005) and parameters and uncertainties as given by Stixrude and Lithgow-Bertelloni (2011). Density and elastic moduli are accurate to within ∼0.5% and ∼1–2%, respectively (Connolly & Khan, 2016). To obtain the mantle pressure profile, we integrate the vertical load from the surface pressure boundary condition. Within the crust and lithosphere, temperature is computed by assuming a conductive geothermal gradient, while the sublithospheric mantle adiabat is defined by the entropy of the lithology at the base of the lithosphere (see Figure S8 for an illustration).

The present thermodynamic model of Stixrude and Lithgow-Bertelloni (2005, 2011) has limitations: (1) the equilibrium assumption is dubious at low temperatures as equilibrium is not likely to be achieved (e.g., Wood & Holloway, 1984). Consequently, we compute mineralogy for temperatures below 500°C at 500°C, and the resultant mineralogy is used to calculate physical properties at the temperature of interest; and (2) the thermodynamic model does not account for redox effects (e.g., Cline II et al., 2018), minor phases, and water and melt due to lack of thermodynamic data. Both, water and melt, can significantly affect elastic

Table 1
Model Mantle Compositions in wt% of Mid-Ocean Ridge Basalt (MORB) and Its Depleted Residue, Harzburgite (from Khan et al., 2009)

Component	MORB, $\mathbf{X}_B$	Harzburgite, $\mathbf{X}_H$
CaO	13.05	0.5
FeO	7.68	7.83
MgO	10.49	46.36
Al_2O_3	16.08	0.65
SiO_2	50.39	43.64
Na_2O	1.87	0.01
Mg#	0.709	0.913

Note. Mg# (molar) is given by Mg/(Mg + Fe).

properties at lithospheric and MTZ depths. Negative gradients in *S* wave velocity (>5%) within the continental lithosphere could arise from hydrous minerals (Green et al., 2010; Rader et al., 2015; Selway et al., 2015) and low wave velocities near the LAB in oceanic and active regions have been attributed to partial melt (e.g., Clark & Lesher, 2017; Karato & Park, 2019; Kawakatsu et al., 2009; Lekić & Fischer, 2014; Rychert & Shearer, 2009; Stern et al., 2015). The MTZ is also considered as a plausible water reservoir within the mantle given the experimentally constrained storage capacities (1–3%) of wadsleyite and ringwoodite (Férot & Bolfan-Casanova, 2012; Kohlstedt et al., 1996; Smyth, 1987). However, mineral physics data suggest the effect of water on seismic velocities is negligible at MTZ conditions as a result of which seismic data are insensitive to water content (Schulze et al., 2018; Thio et al., 2015). While evidence for regional low-velocity layers atop the 410 (e.g., Khan & Shankland, 2012; Kind et al., 2015; Song et al., 2004; Toffelmier & Tyburczy, 2007; Tauzin et al., 2010; Vinnik & Farra, 2007; Xiao et al., 2020), that might be related to partial melt (Bercovici & Karato, 2003; Freitas et al., 2017; Hirschmann, 2006), has been put forward, we find no clear signs for this. Future studies will have to consider this in more detail.

4.2. Crustal Structure

The velocity structure of the crust is important for modeling RFs (see sections S5.1 and S5.3.2). Here, we follow Munch et al. (2018) and model the crust as a stack of three layers of variable thickness and *S* wave velocity, which is assumed to increase with depth. The ratios of density and *P* wave velocity to *S* wave velocity are constant in the crust. We invert for all of these parameters by using conversions at the Moho and Ps crustal reverberations.

4.3. Anelastic Effects

In order to model the effect of anelasticity on seismic amplitudes (K. H. Liu, 2003), we follow the scheme outlined in Munch et al. (2018), which considers a laboratory-based viscoelastic dissipation model derived from grain-size-, temperature-, and pressure-sensitive viscoelastic relaxation measurements. The dissipation model based on the extended Burgers model is described in detail in Jackson and Faul (2010) and relies on laboratory experiments in the temperature range 800°C to 1200°C of torsional forced oscillation data within 1- to 1,000-s period on melt-free poly-crystalline olivine grains between 3- and 165-μm size. Radial profiles of shear attenuation, Q_μ, are determined for the viscoelastic extended Burgers model using the implementation of Bagheri et al. (2019), for which rheological parameters are listed in Table S2.

The advantage of this particular setup is that it allows us to account for, through the thermodynamic interface, the influence of temperature and pressure on the shear attenuation model in a self-consistent manner (Bagheri et al., 2019). Alternative viscoelastic models have also been proposed (e.g., Jackson & Faul, 2010; Karato et al., 2015; Sundberg & Cooper, 2010), but the relatively high-frequency Ps and Sp RFs are not sensitive enough to allow for proper discrimination (see discussion in section S6.3). In case Q_μ exceeds 600, Q_μ is set equal to 600 and bulk attenuation, Q_κ, is held fixed at 57,823 after PREM (Dziewonski & Anderson, 1981).

Table 2
Overview of Model Parameters, Their Quantity, and Prior Model Parameter Ranges and Probability Distributions

Description	Parameter	Quantity	Value/range	Distribution
Basalt fraction	f	1	0–0.5	Uniform
Lithospheric temperature (°C)	T_{lit}	1	950–1600	Uniform
Lithospheric thickness (km)	Z_{lit}	1	70–300	Uniform
Crustal layer thicknesses (km)	δZ	3	1–20	Uniform
S wave velocity of uppermost crustal layer (km/s)	V_S^1	1	2.0–4.1	Uniform
S wave velocity change across Crustal discontinuities (km/s)	δV_S	2	0–0.5	Uniform
Crustal density- and *P*-to-*S* wave	ρ/V_S	1	0.768 ± 0.0213	Normal
velocity ratios	V_P/V_S	1	1.746 ± 0.0195	Normal

5. Inverse Problem

5.1. Formulation of the Inverse Problem

Within the Bayesian framework, the solution to the inverse problem $\mathbf{d} = \mathrm{g}(\mathbf{m})$, where $\mathbf{d}$ is a data vector containing observations and g a typically nonlinear operator that maps a model parameter vector $\mathbf{m}$ into data (Mosegaard & Tarantola, 1995).

$$\sigma(\mathbf{d}, \mathbf{m}) = k \cdot h(\mathbf{m})\mathcal{L}(\mathbf{d}, \mathbf{m}), \tag{4}$$

where k is a normalization constant, $h(\mathbf{m})$ is the prior probability distribution on model parameters (see Table 2) and contains information about model parameters obtained independently of the data under consideration, $\mathcal{L}(\mathbf{d}, \mathbf{m})$ is the likelihood function, which can be interpreted as a measure of misfit between the observations and the predictions from model, and $\sigma(\mathbf{d}, \mathbf{m})$ is the posterior model parameter distribution containing the solution to the inverse problem. The particular form of $\mathcal{L}(\mathbf{d}, \mathbf{m})$ is determined by the observations, their uncertainties, and data noise and will be discussed in the following section.

5.2. Definition of the Likelihood Function

We only consider the time windows that include Ps and Sp RF signal of interest, i.e., converted energy from the Moho (and reverberations thereof), the 410, and the 660 for Ps RFs, and the Moho, the lithosphere, and the 410 for Sp RFs. The windows are determined manually for each stack as illustrated in Figure 5 (gray areas). For each window i, observed RF, and low-pass period T, we consider a L_2-based likelihood function of the form

$$\mathcal{L}_{T,i}^{RF}(\mathbf{d}, \mathbf{m}) = \exp(-\Phi_{T,i}^{RF}), \tag{5}$$

where

$$\Phi_{T,i}^{RF} = \frac{1}{N}\sum_{j}^{N} \frac{||\mathbf{d}_j^{obs} - \mathbf{d}_j^{syn}||^2}{2\sigma_j^2}, \tag{6}$$

with $\mathbf{d}_j^{obs}$, $\mathbf{d}_j^{syn}$, and σ_j being observed and synthetic Ps or Sp RF amplitudes (for a given period and window) and data uncertainty of data point j, respectively, with N denoting the total number of points within each misfit window. Consequently, the total likelihood function for a given station, RF type, and back-azimuth bin is the conjunction of the likelihood functions associated with each period and misfit window:

$$\mathcal{L}(\mathbf{d}, \mathbf{m}) = \prod_{T,i} \mathcal{L}_{T,i}^{RF}(\mathbf{d}, \mathbf{m}). \tag{7}$$

5.3. Sampling of the Posterior

We sample the posterior distribution by means of the Metropolis-Hastings algorithm (Hastings, 1970; Metropolis et al., 1953). This algorithm is based on random sampling of the model space, yet only models that result in a good data fit and are consistent with prior information are frequently sampled (importance sampling). At each step n, a model, $\mathbf{m}^{n+1}$, is proposed on the basis of the prior distribution and is either accepted or rejected based on the probability

$$P = \min\left[1, \frac{\mathcal{L}(\mathbf{m}^{n+1})}{\mathcal{L}(\mathbf{m}^{n})}\right], \tag{8}$$

where $\mathbf{m}^n$ represents the last accepted model. In a slight modification, we use the cascaded Metropolis algorithm (Mosegaard & Tarantola, 1995, 2002), which applies the acceptance criterion (Equation 8) to each period T and misfit window i (crust, lithosphere, 410, and 660) separately for a given station and individual RF type (and back-azimuth bin):

($\star$) propose move: $\mathbf{m}^{n}_{\mathrm{RF}} \longrightarrow \mathbf{m}^{n+1}_{\mathrm{RF}}$ RF=Ps or RF=Sp
for T = 5, 8, 10 s (if RF=Ps) / 10, 15 s (if RF=Sp)
  for i = 1, 2, 3
    if $\mathcal{L}^{\mathrm{RF}}_{\mathrm{T,i}}(\mathbf{m}^{n+1}_{\mathrm{RF}}) \geq \mathcal{L}^{\mathrm{RF}}_{\mathrm{T,i}}(\mathbf{m}^{n}_{\mathrm{RF}})$ then
      accept this step
    else if $\mathcal{L}^{\mathrm{RF}}_{\mathrm{T,i}}(\mathbf{m}^{n+1}_{\mathrm{RF}}) < \mathcal{L}^{\mathrm{RF}}_{\mathrm{T,i}}(\mathbf{m}^{n}_{\mathrm{RF}})$ then decide randomly to move to
      the next step or to reject the proposed move with probability
        $P = \mathcal{L}^{\mathrm{RF}}_{\mathrm{T,i}}(\mathbf{m}^{n+1}_{\mathrm{RF}})/\mathcal{L}^{\mathrm{RF}}_{\mathrm{T,i}}(\mathbf{m}^{n}_{\mathrm{RF}})$
    else reject $\mathbf{m}^{n+1}_{\mathrm{RF}}$ and return to ($\star$)
  end
end

Thus, the model is only retained if all of the individual steps are accepted. This acceptance criterion is more strict when compared to the "standard" acceptance criterion of the Metropolis-Hastings algorithm but acts to prevent trade-offs between misfit windows when considered separately.

Finally, to improve McMC performance, we reduced the burn-in of the sampling stage by employing a global optimisation method in order to obtain a good initial model for the subsequent model space search. For this purpose, we use the Covariance Matrix Adaption Evolution Strategy of N. Hansen and Ostermeier (2001). We first search for a crustal model by minimizing the misfit in the crustal time window and subsequently refine both crustal and thermochemical model by minimizing misfit across all windows. In the McMC stage, we sampled ∼40,000 models in total by running eight chains in parallel, of which ∼4,000 models are retained for analysis here. Step lengths are adjusted so that the acceptance rate is between 30% and 50%. Synthetic test inversions and grid-search examples are described in section S5.

5.4. A Posteriori Migration of Inversion Results

We created a series of maps and cross sections to visualize the spatial variation of model parameters based on mean models. The use of mean models is justified given that the posterior probability density distributions (Figure 6) are mostly Gaussian. Maps and cross sections are produced through linear interpolation of the Ps and Sp RF-derived mean models, which were migrated to their point of sensitivity, which, in the case of Ps RFs, is approximately the location of the station and for Sp RFs is the conversion point of the Sdp phase (cf. section 2.2.3), where d is the depth of sensitivity of a particular model parameter. For example, when migrating Sp RF-derived crustal and lithospheric thickness, d equals either Z_c or Z_{lit}, whereas in the case of temperature, d is equal to 410 km, since thermal information is primarily contained in the S410p phase (see Figure S15).

For a given station, back-azimuth bin, and model parameter with sensitivity d, we compute the coordinates of the Sdp conversion points in IASP91 for all events included in that bin and average them to extract the final point of sensitivity. The so-computed Sp RF points are shown as diamonds in the maps that follow, while Ps RF points, i.e., station locations, are depicted as circles. All estimates related to discontinuity structure (Moho, LAB, and MTZ) have been corrected for station elevation. Finally, while the present inversion is not a tomographic inversion sensu stricto, it is an inversion for a set of (quasi-local) radial profiles of thermochemical and physical structure, which, when pieced together, result in tomographic images that are based on the a posteriori migration procedure.

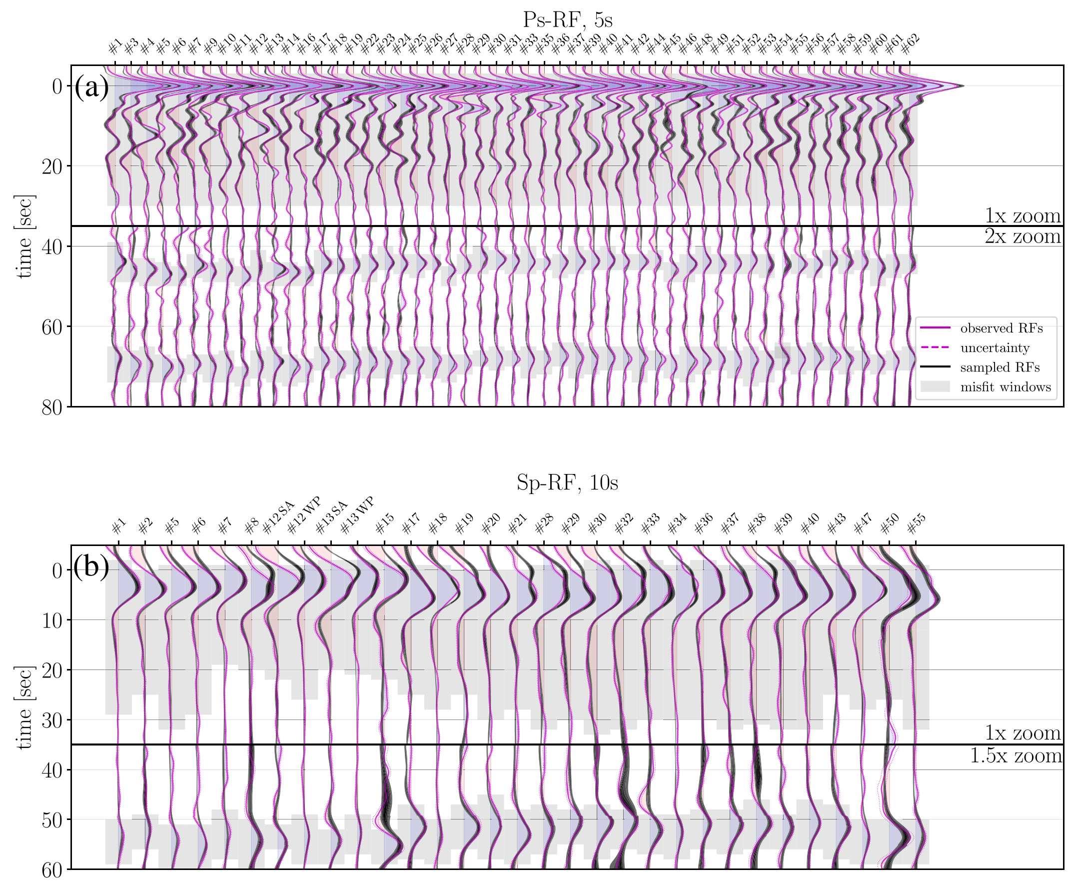

Figure 5. Data misfit between inverted and observed high-quality (a) Ps (5s low-pass period) and (b) Sp receiver functions (10s low-pass period). Observations and uncertainties are shown as magenta lines, sampled receiver functions as contours (dark bands), and misfit windows in light gray. Station numbering is shown in Figure 2c, whereas "SA" and "WP" denote events located in South America and the West Pacific, respectively. For improved visibility, amplitudes of conversions from the 410 and 660 have been scaled up. Equivalent data fits for Ps and Sp receiver functions at low-pass periods of 8-, 10-, and 15-s are shown in Figure S19.

6. Results and Discussion

6.1. Datafit

The fits to observed Ps and Sp RFs at 5- and 10-s period, respectively, are shown in Figure 5. Fits to Ps and Sp RFs at the other periods are summarized in Figure S19. Conversions at the Moho, 410, and 660 discontinuities as well as lithospheric Sp RFs are seen to be captured well by the sampled models.

6.2. Crustal Thickness

The inverted mean crustal thickness model is shown in Figure 7a. Results for ρ/V_S and V_P/V_S can be found in Figure S20. The abbreviations and extent of physiographic and tectonic provinces referred to hereafter are depicted in Figures 2a and 2b. As expected, crustal thickness estimates are better constrained from Ps than from Sp RFs (Figures 6a and 6b) given the higher frequency content of Ps RFs and the additional information contained in crustal reverberations. Mean Ps and Sp RF-derived standard deviations are 1.6- and 3.5-km, respectively. For comparison, we are also showing the crustal thickness map based on Crust1.0 (Laske et al., 2013) in Figure 7b. Our model is in good agreement with Crust1.0, including other models (not shown; e.g., Buehler & Shearer, 2017; Lowry & Peréz-Gussinyé, 2011; Levander & Miller, 2012; Ma & Lowry, 2017; Schmandt et al., 2015; W. Shen & Ritzwoller, 2016) that indicate that regions with relatively thin crust (25–35 km) are found in the western part of the United States, i.e., beneath the Columbia plateau (physiographic province P2) and the Basin and Range province (P3), as well as the passive margins of the continent in the southern and eastern parts (P10). Regions with thicker crust (45–55 km) are observed underneath the Wyoming craton (tectonic province T2) and Trans-Hudson orogen (T3) as well as within the

10.1029/2020JB020350

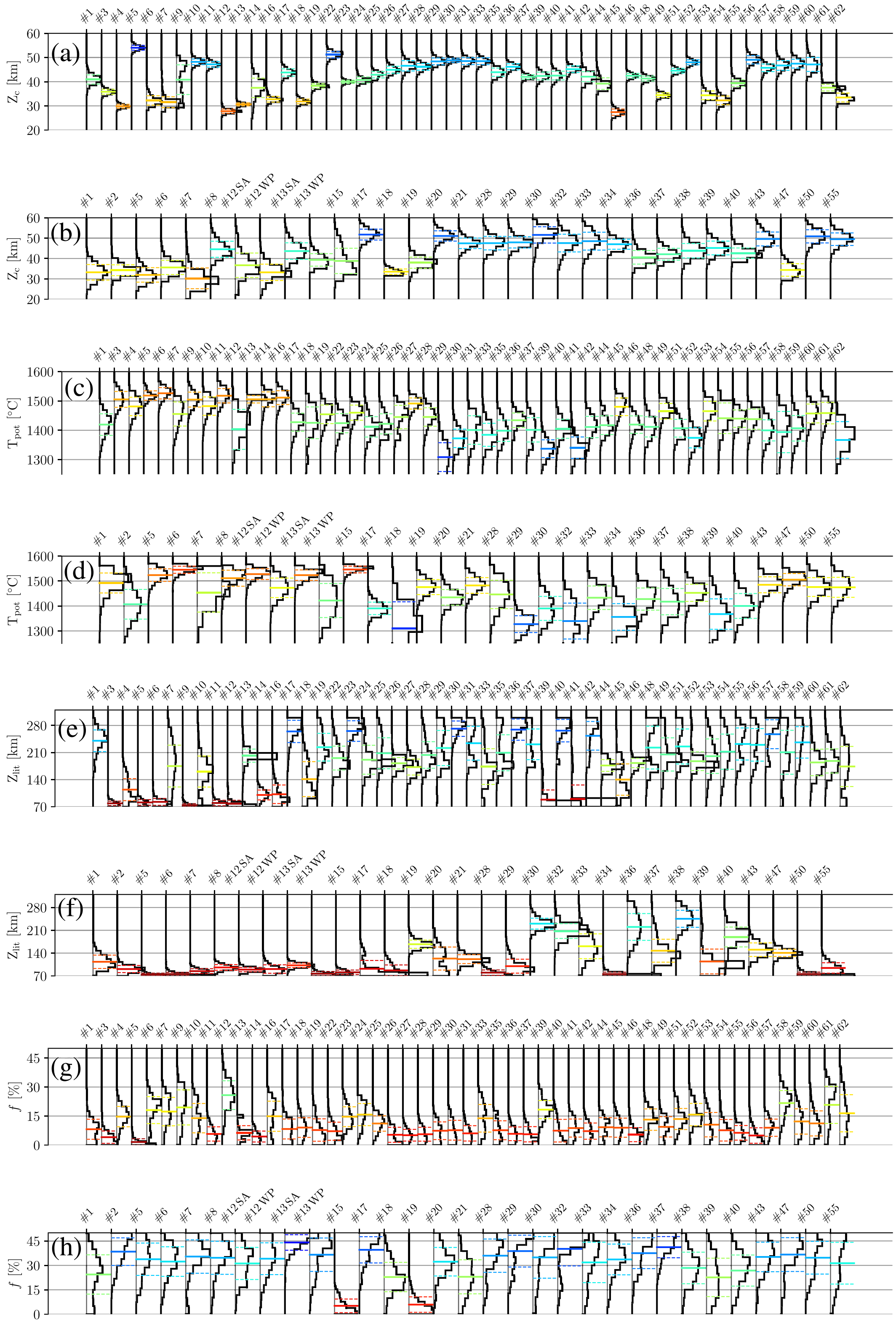

Figure 6. Sampled marginal posterior probability distributions (black lines) of (a and b) crustal thickness, Z_c, (c and d) potential temperature, T_{pot}, (e and f) lithosphere thickness, Z_{lit}), and (g and h) basalt fraction, f, from inversion of Ps and Sp receiver functions, respectively. Mean values and standard deviations of the distributions are shown as thick and thin lines, respectively, where choice of color is based on the colormaps used in Figures 7 and 9. Station numbering refers to Figure 2c, whereas "SA" and "WP" refer to events from South America and the West Pacific, respectively.

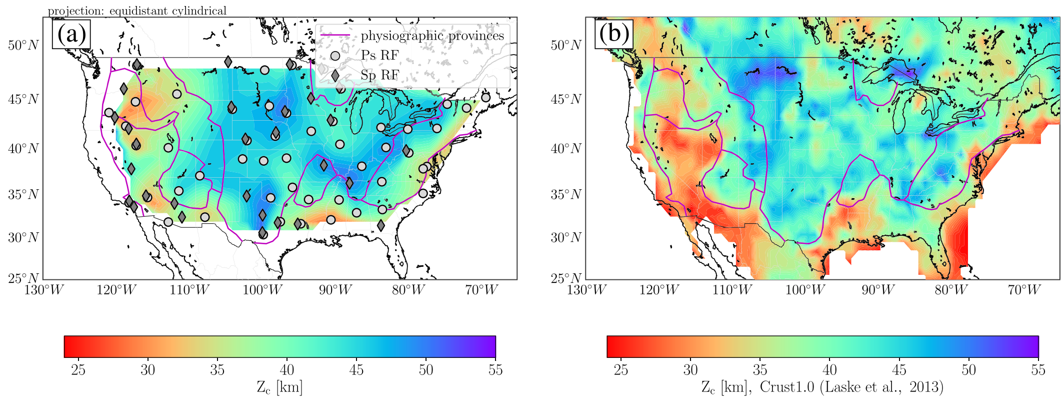

Figure 7. (a) Mean crustal thickness, Z_c, across the contiguous United States interpolated from migrated Ps (circles) and Sp (diamonds) receiver functions. (b) Crustal thickness map from model Crust1.0 (Laske et al., 2013). Physiographic provinces are outlined in magenta (Fenneman, 1928, cf. Figure 2a).

precambrian building blocks towards the east (P6–P8; T4–T8) and south-west that extend into the Colorado plateau (P4).

6.3. Tectonic Regionalization

In order to embed the results in a geologic context, we first extracted radial profiles of temperature, S wave velocity, and shear attenuation on a $2.5° \times 2.5°$-grid and grouped them individually via k-means clustering according to their similarity, i.e., by minimizing the L_2 distance to the mean profile of the respective cluster (MacQueen, 1967). This approach allows for identification of tectonic regions without any a priori constraints (e.g., Calò et al., 2016; Houser et al., 2008; Lekić & Romanowicz, 2011; Lekić et al., 2012). Consistent results were found for three clusters that are shown in Figure 8. The radial profiles for each parameter show specific characteristics that determine the clustering: (1) temperature and depth of the intersection point of conductive geotherm and mantle adiabat; (2) amplitude and depth extent of upper mantle low-velocity zone; and (3) thickness of the high-Q_μ lid.

When the mean profile for each location is projected onto a map (see insets in Figure 8), a well-known trend that follows the tectonic division of the North American continent appears. In particular, we are able to distinguish the tectonically active west (encompassing physiographic provinces P1–P5), which is characterized by being relatively hot, of slow shear-wave velocity, and highly dissipative (red dots), from the colder, faster,

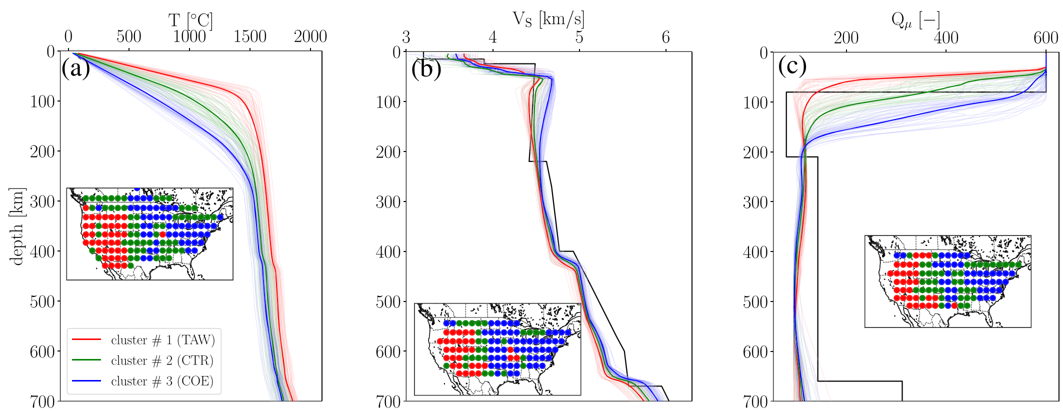

Figure 8. Profiles of (a) temperature (T), (b) S wave velocity (V_S), and (c) shear attenuation (Q_μ) obtained from inversion of Ps and Sp receiver functions and clustering analysis. Profiles are grouped into three clusters according to similarity (color coded) and displayed in light color, whereas the mean profile of each cluster is shown as a thick line. The tectonic regions identified in panel (a) will be referred to as tectonically active West (red; TAW), central transition region (green; CTR), and cratonic-orogenic East (blue; COE) in the following. The maps shown in the insets are interpolated from the inversion results on a $2.5° \times 2.5°$-grid. PREM profiles are shown in black in panels (b) and (c).

Table 3
Summary of Thermochemical Characteristics and Discontinuity Structure of the Main Tectonic Regions Identified Through Cluster Analysis in Figure 8a

	Tectonic region		
Parameter	TAW (tectonically active West)	CTR (central transition region)	COE (cratonic-orogenic East)
Z_c	40 ± 5 km	44 ± 5 km	44 ± 4 km
T_{pot}	1490 ± 27°C	1429 ± 37°C	1413 ± 27°C
Z_{lit}	100 ± 23 km	146 ± 31 km	208 ± 33 km
f	$13 \pm 4.5\%$	$11 \pm 3.0\%$	$10 \pm 3.6\%$
Mg#	0.904 ± 0.003	0.906 ± 0.002	0.907 ± 0.003
Z_{410}	424 ± 7 km	417 ± 6 km	416 ± 6 km
Z_{660}	660 ± 2 km	659 ± 2 km	658 ± 2 km

Note. Parameters are crustal thickness (Z_c), potential temperature (T_{pot}), lithosphere thickness (Z_{lit}), basalt fraction (f), Mg# (molar Mg/(Mg + Fe)), and depth to 410 (Z_{410}) and 660 (Z_{660}). Values represent the mean and standard deviation based on the distributions shown in Figures 9c, 9e, 12b, and 12d.

and less dissipative older eastern parts (blue dots) that include the cratonic core and the Appalachian mountains, i.e., parts of provinces P6–P9 and T2–T8. The third cluster (green dots) represents an intermediate group of profiles distributed over the central and eastern parts that are sandwiched between red and blue regions. While these features suggest that tectonic regions are mainly controlled by the thermal structure of the continental lithosphere, a compositional signal is also present (section 6.6). For the remainder of the discussion, we will refer to the tectonic regions identified in Figure 8a as the tectonically active West (TAW; red), the central transition region (CTR; green), and the cratonic-orogenic East (COE; blue). Smoothed outlines of these regions are indicated in the maps and an overview of the values observed for the thermochemical parameters is given in Table 3.

6.4. Mantle Temperature

For ease of comparison with literature estimates, we rely on the concept of potential temperature, T_{pot}, which is the temperature of the adiabatic mantle when extended to the Earth's surface (McKenzie & Bickle, 1988). We compute T_{pot} by linear extrapolation of the adiabatic mantle geotherm: $T_{pot} = T_{lit} - \nabla T \cdot Z_{lit}$, where we have employed an adiabatic gradient $\nabla T = (T_{410} - T_{lit})/(Z_{410} - Z_{lit})$ with T_{410} and Z_{410} representing temperature at and depth of the 410, respectively. Uncertainties on T_{pot} average 35°C and 43°C for Ps and Sp RFs, respectively (Figures 6c and 6d). Figure 9a displays interpolated mean values of T_{pot}. As in Figure 8a, we observe a clear east-west trend from low to high potential temperatures, reaching values of 1430°C to 1520°C in region TAW, 1360°C to 1470°C in CTR, and 1350°C to 1450°C in COE, respectively. We find large positive thermal anomalies underneath the Cascade range (P1), the Basin and Range province (P3), and Yellowstone Hotspot. The same general east-west pattern was also observed in the thermal anomaly maps obtained by Khan et al. (2011) from inversion of surface wave phase velocities, although of lower resolution, by Maguire et al. (2018) from stacking of Ps RFs, and S. M. Hansen et al. (2015) from analysis of surface wave tomographic models. We should note that thermal anomalies constrained by Sp RFs could be biased by the basalt-rich nature of the inverted compositions (see Figure 6h). We estimate that in these regions, "normal" basalt fractions would cool the mantle locally by up to ~30°C to 50°C (cf. Figure S16).

6.5. Lithospheric Thickness and Structure

A map of the thickness of the thermal lithosphere is shown in Figure 9b. We emphasize that lithospheric thickness refers to the depth (defined by Z_{lit}) at which the conductive geotherm intercepts the mantle adiabat. There is no apparent discontinuity associated herewith and hence no converted phase; yet the

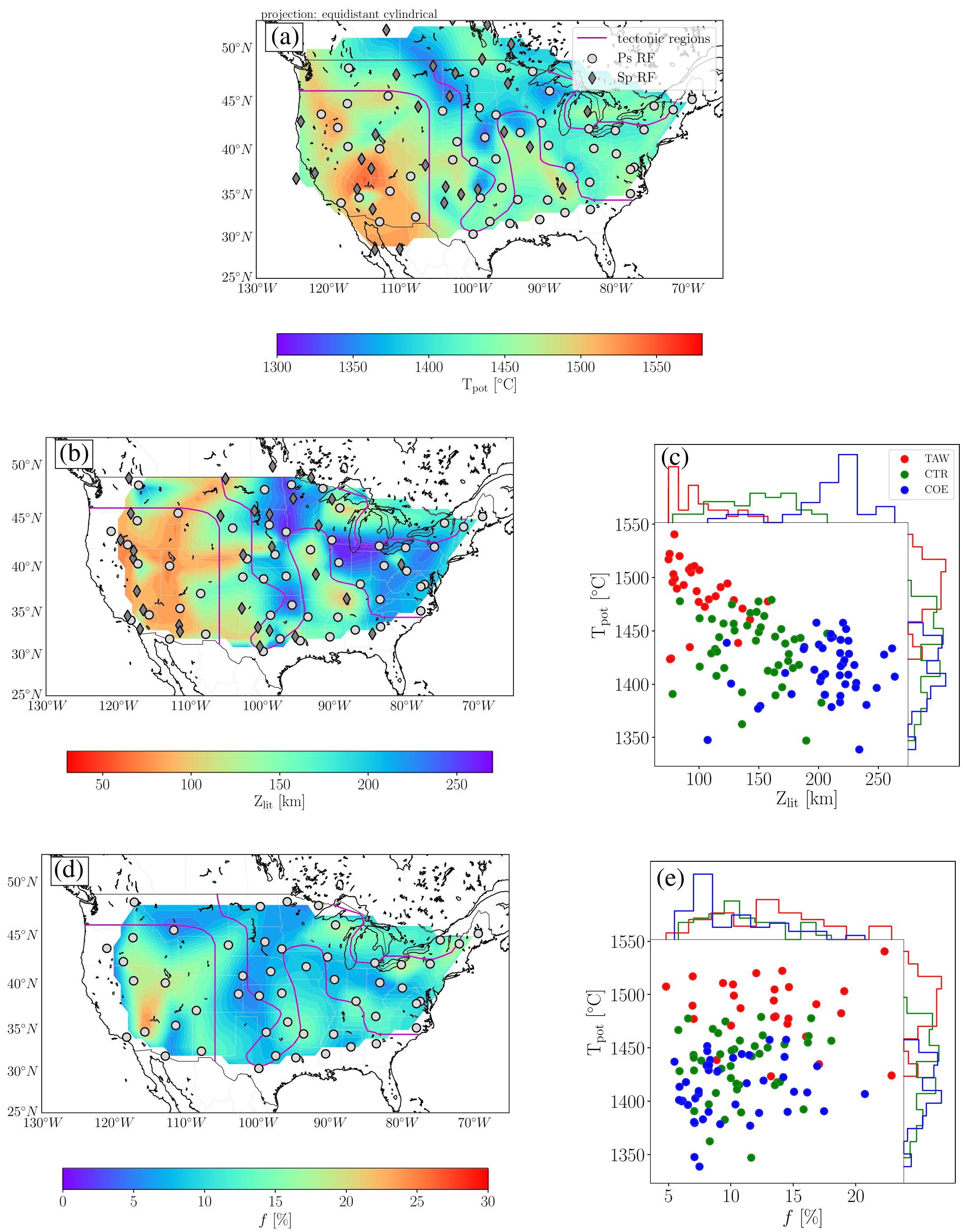

Figure 9. Models of the North American thermochemical mantle structure: (a) potential temperature, T_{pot}, (b) lithosphere thickness, Z_{lit}, and (d) basalt fraction, f. Tectonic regions identified earlier (cf. Figure 8a) are outlined in magenta. The distribution and correlation of T_{pot} with Z_{lit} and f for each of these tectonic regions (color coded) are shown in panels (c) and (e), respectively. Maps derive from Ps (circles) and Sp (diamonds) receiver functions, respectively, except the compositional map showing basalt fraction (d), where Sp receiver function estimates are excluded because of the large uncertainties (see section 6.6). Differences in lateral extent of these maps arise from the migration of Sp receiver function results along the converted raypath to different depths (see section 5.4).

long-period part of the Sp RFs (cf. Figure S15) is affected. Note that uncertainties on thermal lithospheric thickness are generally much smaller for Sp (17 km) than for Ps RFs (32 km) (Figures 6e and 6f). This arises because lithospheric Sp RFs are not obscured by crustal reverberations, as is the case for Ps RFs. Consequently, Ps RFs only provide indirect insight into lithospheric structure via the sensitivity of the P410s and P660s to mantle temperature, which is controlled by both Z_{lit} and T_{lit}. However, as Sp measurements are sparse, we include the results from Ps RFs for interpolating Z_{lit}.

The thinnest lithosphere (79–141 km) is found in region TAW, as also observed in previous studies that considered Ps and/or Sp RFs (e.g., Abt et al., 2010; S. M. Hansen et al., 2015; Hopper et al., 2014; Li et al., 2007; Lekić et al., 2011; Levander & Miller, 2012). The exact shape of the thin-lithosphere branches that extend across the Rocky Mountains (P5) towards the Central plains (P6) are only constrained by few data points and hence are not interpreted further here. Region CTR shows an intermediate range in lithospheric thickness of 85–187 km and coincides mostly with the western Great plains (P6), the New Madrid Seismic Zone (e.g., C. Chen et al., 2014; Zhang et al., 2009), and the mid-continental rift system (e.g., Stein et al., 2015). Finally, region COE is, as expected on account of its cratonic and orogenic nature, composed of relatively thick lithosphere (125–247 km). This negative correlation between potential temperature and lithospheric thickness observed in the maps is clearly visible in Figure 9c and is further illustrated in the tomographic cross sections shown in Figure 11, where lateral variations in thickness go hand-in-hand with variations in *S* wave anomalies (see section 6.7) such that thick lithosphere is predominant in "cold" regions, whereas thin lithosphere is found in "hotter" regions.

We should note that some Sp RFs (e.g., 17-JCT, 32-SUSD, and 39-COWI) show complexities in the lithospheric part that are difficult to fit, which could potentially lead to a bias in thermal thickness estimates. These complexities have been attributed to mid-lithospheric discontinuities (MLDs) that were observed in Sp RFs from North America (e.g., Abt et al., 2010; Calò et al., 2016; Miller & Eaton, 2010; Kind et al., 2015; Lekić & Fischer, 2014; H. Yuan and Romanovicz, 2010) and elsewhere (e.g., L. Chen, 2009; Ford et al., 2010; Heit et al., 2007; Sodoudi et al., 2013; Savage & Silver, 2008; Wölbern et al., 2012). Processes capable of creating MLDs have been discussed extensively by Selway et al. (2015). In a recent study, Kind et al. (2020) has pointed out that MLDs could result from the use of "inexact" filtering and deconvolution. Instead of deconvolution, Kind et al. (2020) directly summed waveforms to obtain RF stacks. The resultant MLDs were less apparent and point to the importance of careful data processing. The exact nature of data processing is of less importance in our study, inasmuch as the problems that beset imaging and interpretation are avoided in an inversion, where the same processing steps are applied to synthetic and observed data.

6.6. Mantle Composition

Mantle composition (basalt fraction) primarily affects the sharpness of the 410 and 660 seismic discontinuities through its influence on RF amplitudes rather than the timing of converted waves (see Figure S15). This is opposite to the effect of temperature, which primarily affects the depth of the 410 and 660 and, through that, travel time of the converted phases. This separation of sensitivity allows us to decouple the parameters. Basalt fractions estimated from Ps RFs vary on average from 0% to 25%, i.e., within the harzburgite to pyrolite range with uncertainties around 5% (cf. Figure 6g). In comparison, Sp RF-estimated basalt fractions show larger uncertainties (9.5%; cf. Figure 6h) and appear to cluster toward the upper end of the prior ($f = 50\%$), in disagreement with the Ps RF-derived results and other studies (e.g., Khan et al., 2011; Maguire et al., 2018). The inferred basalt enrichment is likely related to the reduced sensitivity of the S410p to composition, because of the generally small amplitudes of S410p relative to P410s. However, as noted earlier, this only has a small effect on thermal estimates due to the first-order decoupling of temperature and composition. Consequently, we exclude Sp RF-derived information from the compositional map (Figure 9d).

For present purposes, we express composition by means of the Mg#, which is computed as Mg/(Mg + Fe) (molar), where high/low Mg# is indicative of depleted/fertile mantle, i.e., low/high basalt fraction, respectively (cf. Table 1). While most of the mantle across the continent appears to be made up of relatively depleted compositions (Figure 9d), region TAW is found to be slightly more fertile ($f = 13 \pm 4.5\%$, Mg# ~ 0.90) in comparison to regions CTR and COE (COE: $f = 10 \pm 3.6\%$, Mg# ~ 0.91), similar to the results of Khan et al. (2011). Local enrichment of basalt underneath the continent could correspond to traces of active (Cascadia) and ancient subduction zones (Farallon). The location of these anomalies are in agreement with the results by Maguire et al. (2018).

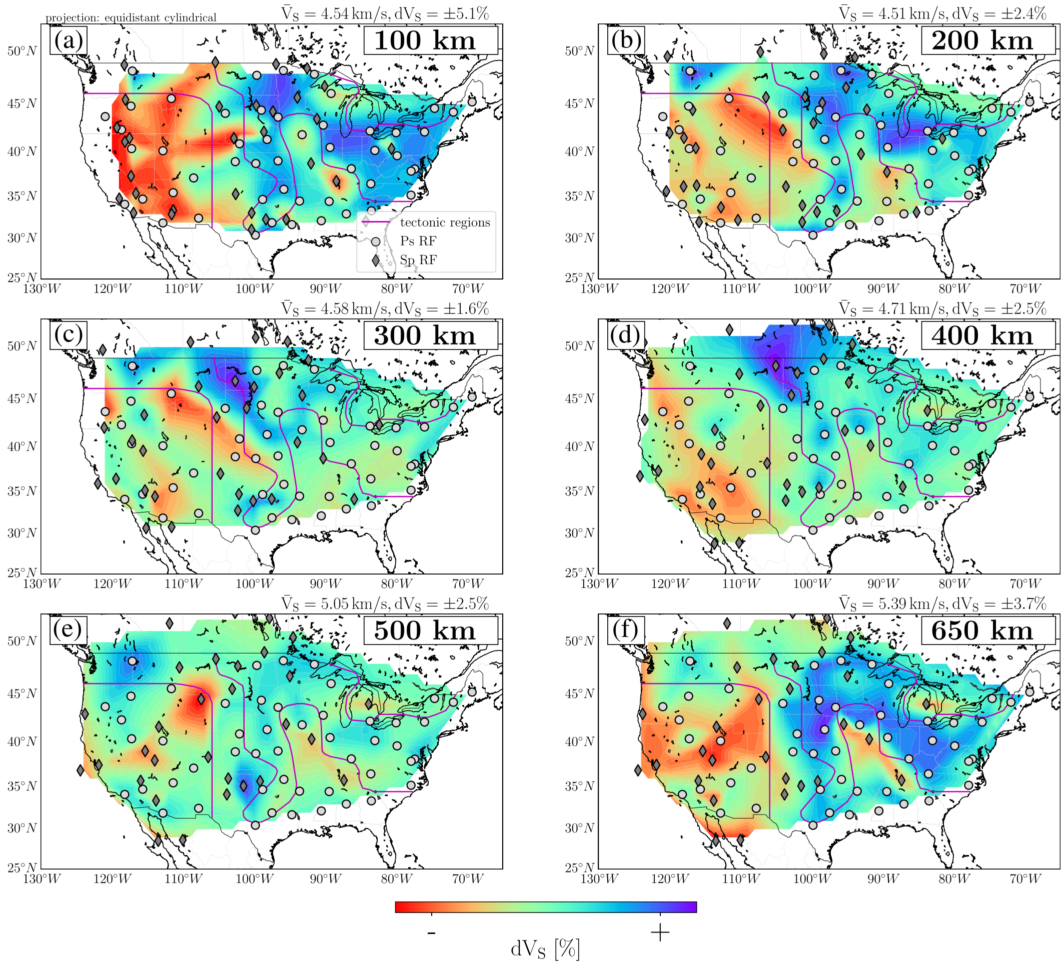

Figure 10. Interpolated *S* wave velocity perturbations, dV_S, along horizontal slices between 100- and 650-km depth. All maps share the same colormap but differ in absolute mean velocity and standard deviation (indicated on the top right of each panel). Earlier identified tectonic regions (cf. Figure 8a) are outlined in magenta. Differences in lateral extent of these maps arise from the migration of Sp receiver function results along the converted raypath to different depths (see section 5.4).

6.7. Shear-wave Velocity Structure

In the following, we focus on models of isotropic elastic *S* wave velocity. Figure 10 shows *S* wave velocity images of the upper mantle and MTZ. For comparison, analogous plots for two tomographic models, US-SL-2014 (Schmandt & Lin, 2014) and SL2013NA (Schaeffer & Lebedev, 2014), are shown in Figures S22–S25). To illustrate lateral variations in structure further, we also present cross sections (Figure 11) along three east-west and north-south profiles (magenta lines in Figure 2c). From these tomographic images, the following observations can be made:

1. *S* wave velocity anomalies in the upper mantle (100–300 km) closely follow the tectonic regionalization and appear to be dominated by the lithospheric signature in that velocities are high/low in regions with a deep/shallow lithosphere, respectively. These observations are particularly apparent in the east-west trending cross sections, where the lithosphere slowly thickens and *S* wave velocities decrease when passing from region TAW to CTR underneath the eastern Rocky Mountains flank (P5 to P6). The large variations in lithosphere thickness (70–250 km) affect the extent and amplitude of the upper mantle low-velocity zone (Figure 8b), including large lateral velocity variations of ±5.1% at 100-km depth. Amplitudes aside, similar observations were made in models SL2013NA and US-SL-2014 (Figures S22–S25) and other regional tomographic models (e.g., Bensen et al., 2009; Grand & Helmberger, 1984; Khan et al., 2011; Krischer et al., 2018; W. Nettles & Dziewonski, 2008;

Shen & Ritzwoller, 2016; van der Lee & Frederiksen, 2005; Yuan & Romanovicz, 2010; Yuan et al., 2011, 2014).

2. We are able to image mantle features underneath the western margin of the continent (region TAW), where volcanism, accretion, and extensive tectonics are the likely surface expression of ancient and active subduction (e.g., Dickinson, 2004; Humphreys, 2009; Sonder & Jones, 1999). We observe localized high-velocity anomalies in the north that move further inland and southward at greater depths (Figure 11b) and probably represent fragmented pieces of the Juan de Fuca, Gorda, and Farallon slabs (e.g., Portner & Hayes, 2018; Sigloch, 2011). We further see a dominant low-velocity band parallel to the Pacific coast, which, at shallow depths, forms a circular structure around the Colorado plateau (P4) that extends towards Yellowstone. Similar features were identified by Becker (2012) in a comparison of tomographic models of the region (Burdick et al., 2008, 2010; James et al., 2011; Obrebski et al., 2010, 2011; Roth et al., 2008; Schmandt & Humphreys, 2010, 2011; Sigloch, 2011). However, it has to be pointed out that (1) resolution of our model is low because of reduced data coverage at shallow depth at the flank of the eastern Rocky Mountains (P5) and (2) high basalt fractions, as inferred from Sp RFs, tend to decrease velocity within the MTZ, which exaggerates low-velocity anomalies in regions where Ps RF data points are limited.
3. Considering the central and eastern part (regions CTR and COE), we find multiple high-velocity anomalies that extend to the MTZ, where a roughly north-south aligned band underneath the Great plains (P6) is the most pronounced feature (see east-west cross section). These anomalies could be interpreted as remnant pieces of the Farallon or Laramide slabs, although differences in shape relative to other studies are apparent (e.g., Porritt et al., 2014; Sigloch, 2011; Schmandt & Lin, 2014).
4. Toward the bottom of the upper mantle, amplitudes of shear-wave anomalies generally decrease but again increase significantly at and around 400-km depth as olivine transforms to wadsleyite. Lateral velocity variations are larger than those above and below the transition and emphasizes the importance of considering phase-induced variations in addition to variations arising purely from volumetric velocity perturbations. Structure in and around the MTZ is complex and shows significant topography, particularly on the 410 (Figure 12a). As shown in Figure 12b, we find that the 410 occurs deeper (409–432 km) in "hot" regions (TAW) than in "colder" parts (404–423 km in CTR; 401–422 km in COE). To compositionally achieve an equivalent 410-depth variation (>30 km), basalt fraction would have to change by >50% (see Figure S16), which corresponds to more than the total compositional variation observed across the whole study area (Figure 9d). This suggests that composition is of secondary nature in determining topography on the 410.
5. In contrast to the large peak-to-peak amplitudes of >30 km for the 410, lateral variations of the 660 are only ±5 km (Figure 12c) and there appears to be little correlation with temperature (Figures 12d). Instead, the dependence of the 660 on temperature and composition is highly nonlinear (Figure S14) and also affected by the transformation of garnet, whose relative importance increases as temperature and basalt fraction increases (e.g., Hirose, 2002; Khan et al., 2009; Weidner & Wang, 1998; Xu et al., 2008) (see also Figures S3 and S4 of Munch et al., 2018). Since the Clapeyron slopes for the transformations of garnet and ringwoodite are opposite in sign (Hirose, 2002; H. Liu et al., 2018), the garnet phase transition would follow the behavior of the 410 and move deeper in regions of elevated temperature.
6. MTZ thickness (Figure 12e) is largely controlled by the topography on the 410 and is thinner in region TAW (∼220–250 km) than in CTR and COE (∼230–260 km). The 410 beneath the western United States (TAW), where two strong depressions separated by a high-elevation band across northern Nevada (see Figure 11b) are observable, agrees well with other Ps and Sp RF studies of the region (Cao & Lavender, 2010; Gao & Liu, 2014; Tauzin et al., 2013) and possibly relates to subduction. In contrast, the 660 and hence MTZ thickness varies more across the aforementioned studies. This first and foremost reflects the use of different imaging methods and different reference models to convert RFs from time to depth. Furthermore, to the east of the Rocky Mountain front (CTR and COE), our inferred 410 and hence MTZ thickness tends to "normal" values, in overall agreement with the continental-scale MTZ model of Gao and Liu (2014). Further to this, Gao and Liu (2014) found, in agreement with Maguire et al. (2018), the MTZ to be locally thicker underneath the Great Plains (P6), which they attributed to remnants of the Farallon or Laramide slabs. Although less prominent, similar MTZ anomalies are also observed here.

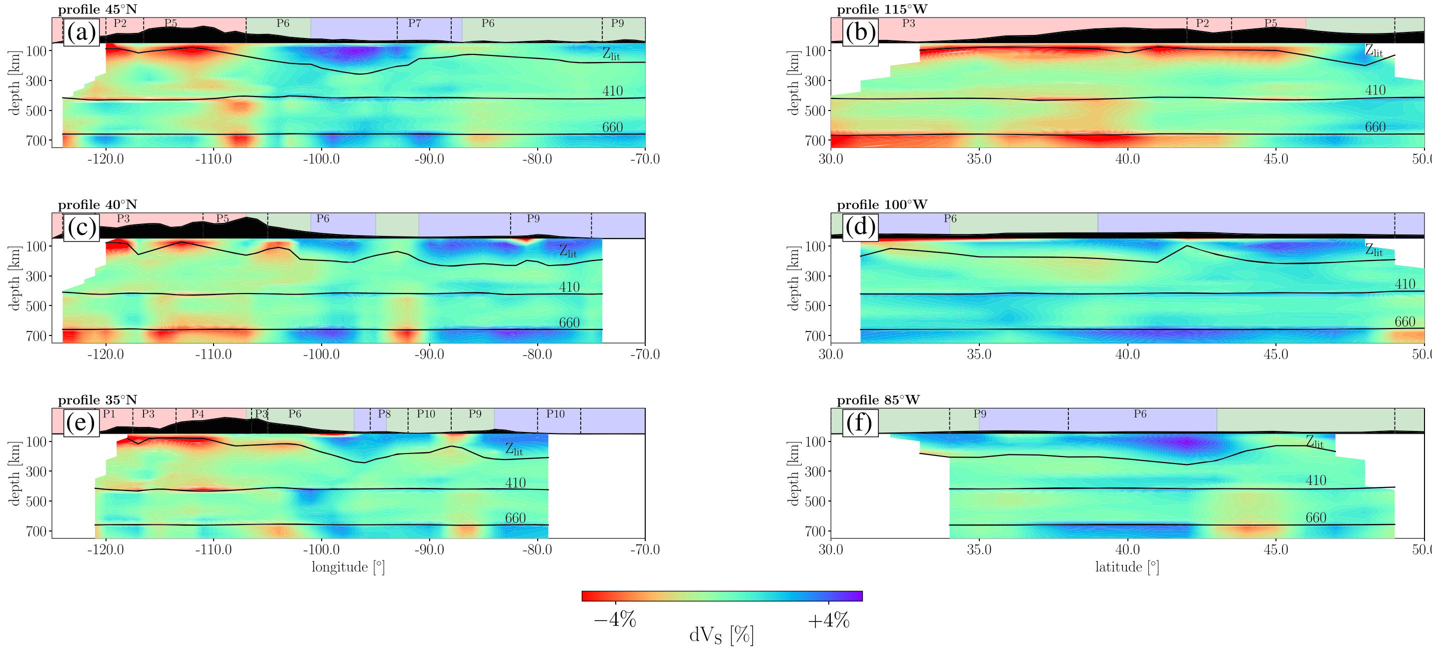

Figure 11. (a, c, and e) Longitudinal cross sections of *S* wave velocity perturbations at 45°N, 40°N, and 35°N latitude, respectively, and (b, d, and f) latitudinal cross sections at 115°W, 100°W, and 85°W longitude, respectively. Lines indicating location of cross sections are shown in Figure 2c. The perturbation is computed relative to the mean velocity with depth (not shown). Surface topography (Laske et al., 2013) is exaggerated 50× and black lines represent topography on lithosphere and 410- and 660-km seismic discontinuities. Differences in lateral extent with depth arise from the migration of Sp receiver functions along the converted raypath to different depths (see section 5.4). Above each panel, the extent of the tectonic regions identified in Figure 8a are indicated by different colors: TAW (red), CTR (green), and COE (blue). Physiographic provinces (Fenneman, 1928, cf. Figure 2a) are outlined with dashed vertical lines.

7. Comparison of Seismic and Thermobarometric Constraints

Assessment of the chemical and petrological characteristics of erupted lavas can provide complementary information to seismic inversions to understand the thermochemical structure of the underlying mantle. In order to facilitate this comparison, we compiled whole rock chemical analyses of ∼500 primitive basaltic rocks from the western United States, filtered for basalts with eruption ages younger than 5 Ma and with MgO contents ≥8 wt% (see section S7 for details). The composition of each sample was inverted in order to solve for the mean pressure and temperature of melt segregation according to the thermobarometer of Lee et al. (2009) to create an internally consistent database. The resultant estimates on (minimum) lithosphere thickness and mantle potential temperature for each sample have uncertainties of about 17 km and 50 °C, respectively. Our results are consistent with those of Plank and Forsyth (2016) to within ±20°C and ±15 km for overlapping localities.

Comparison between petrological and seismological T-P estimates is subject to caveats associated with (i) the differing spatial coverage and (ii) the degree to which phase and/or compositional changes influence the seismic inversion (section 4.1). To account for the locally confined spatial sensitivity of thermobarometry relative to seismic wavelengths (cf. section 2.2.3), we masked cells beyond a radius of 1.5° to a sample location. Lithospheric thickness is more difficult to compare given the reduced data coverage in the western-most United States and the imposed seismic lower bound of 70 km.

With these considerations in mind, the interpolated results from thermobarometry are shown in Figures 13a and 13b, while the difference to seismically derived potential temperature estimates are presented in Figures 13c and 13d. The major magmatic provinces are demarcated on the basis of both seismic and petrological inversions (Figures 9 and 13). Thermally anomalous mantle is observed underneath the Cascade range (northern P1) and the Snake River Plain (eastern P2) towards Yellowstone Hotspot, and particularly under the Basin and Range province (P3) in southern Nevada, extending towards the southeast in the Rio Grande rift. Both methods agree on the relative amplitude of thermal anomalies, but differ in absolute values.

The largest temperature discrepancies, in which seismological estimates are 100°C to 250°C higher with respect to thermobarometric inversions (cf. Figures 13c and 13d), are primarily observed along the Cascade

10.1029/2020JB020350

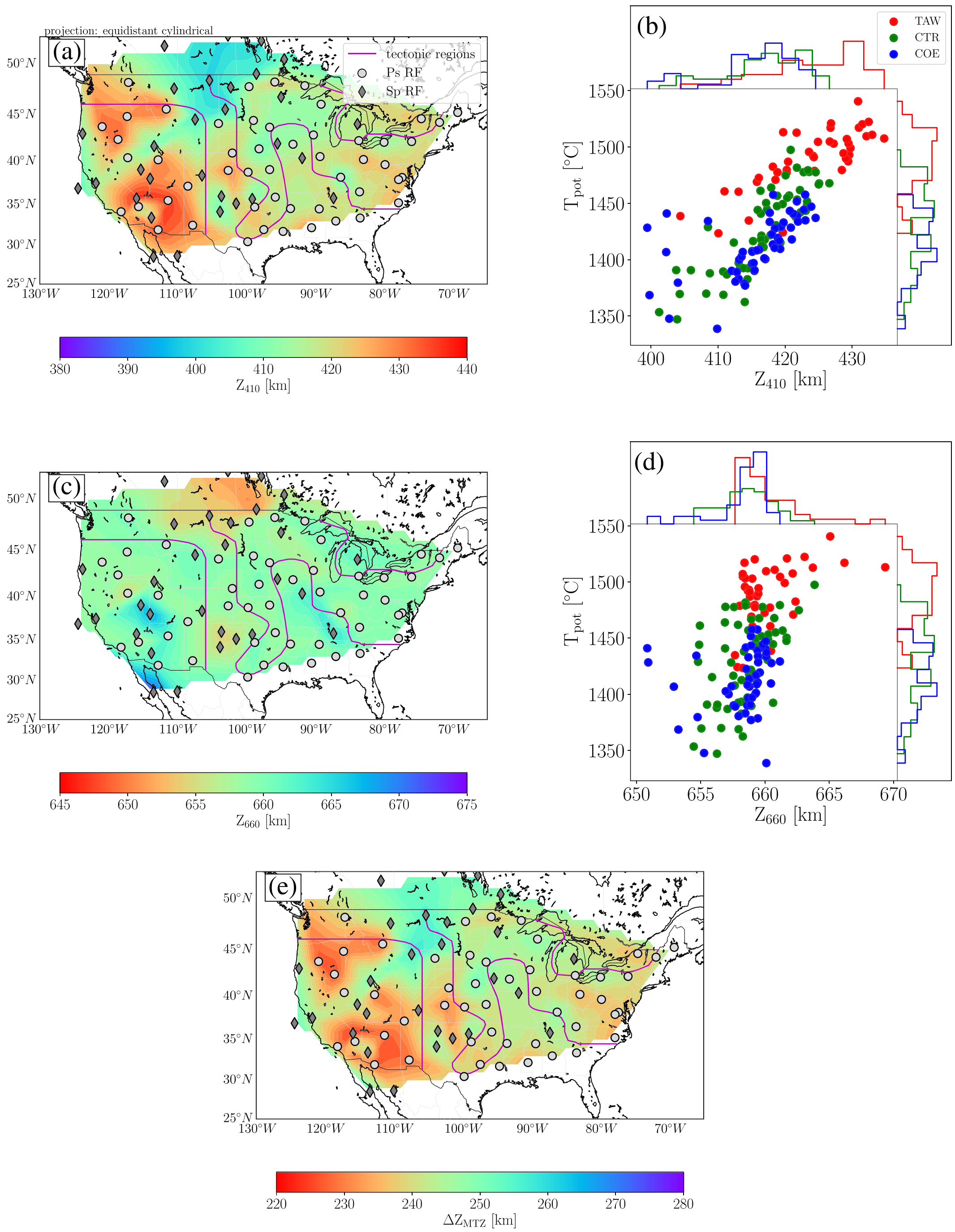

Figure 12. Interpolated maps of mean depth to the major mantle seismic discontinuities at 410- and 660-km depth, (a) Z_{410}, (c) Z_{660}, and (e) mantle transition zone thickness, ΔZ_{MTZ}. Tectonic regions identified in Figure 8a are outlined in magenta. The distribution and correlation of mantle potential temperature T_{pot} with Z_{410} and Z_{660} for each of these regions (color coded) is shown in panels (b) and (d), respectively.

arc parallel to the Pacific coast (P1). The petrologically derived potential temperatures, 1300°C to 1350°C, are in agreement with other thermobarometric estimates (Grove et al., 2002; Leeman et al., 2005), whereas temperatures derived from the seismic model may reflect the cumulative effects of increased H_2O, fO_2, and melt fraction underneath this region, none of which are considered. Influx of water and oxidizing melts from the downgoing slab into the mantle wedge are characteristics of subduction zones, with the net effect being

10.1029/2020JB020350

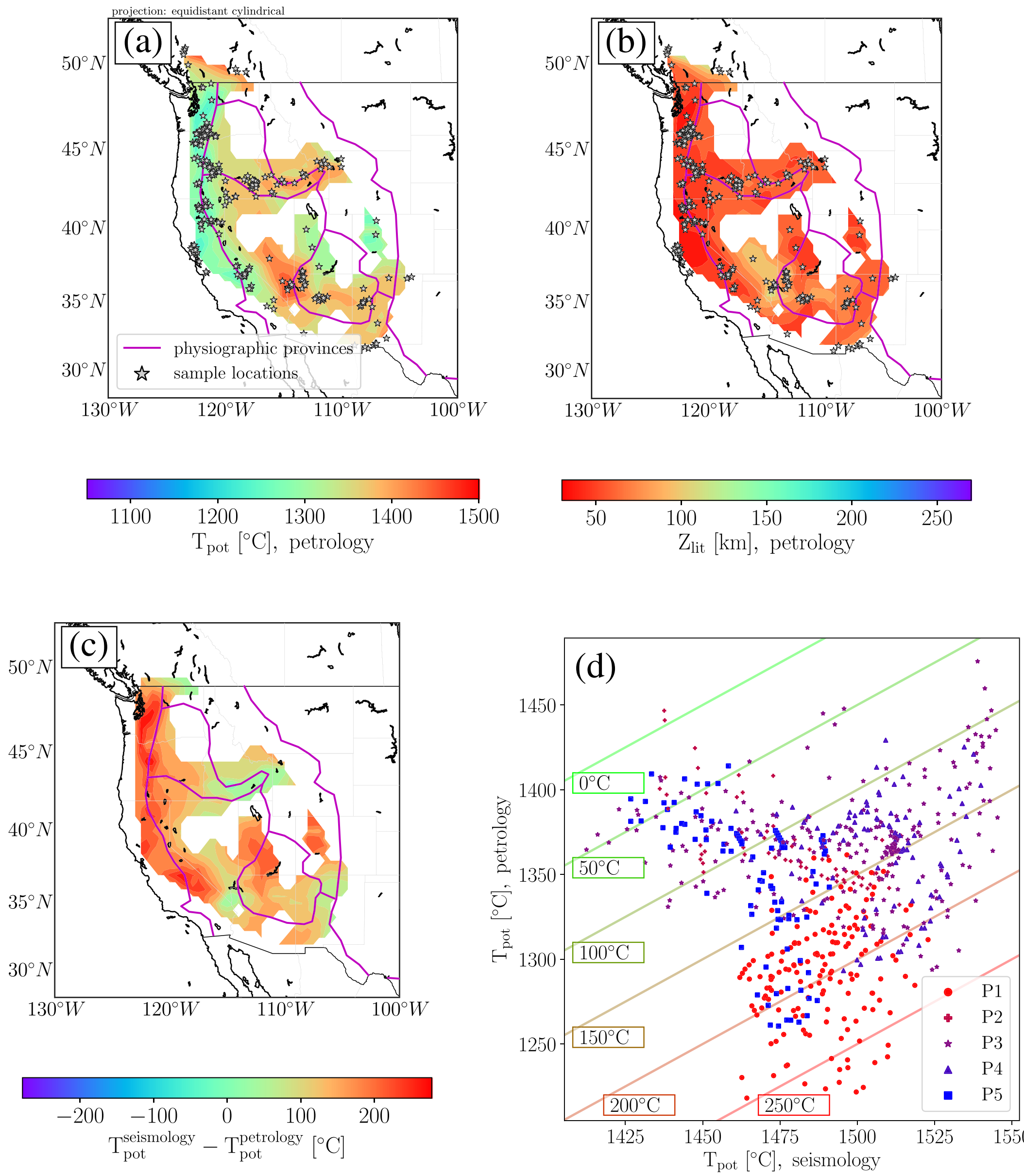

Figure 13. Thermochemical structure of the lithosphere underneath the western United States as estimated from thermobarometry: (a) interpolated potential temperature (T_{pot}) and (b) lithosphere thickness (Z_{lit}). The deviation to seismically derived temperature estimates (cf. Figure 9a) is shown in panel (c). Cells of the interpolation grid farther away than 1.5° from the nearest sample location (stars) are masked. Physiographic provinces are outlined in magenta (Fenneman, 1928, cf. Figure 2a). Panel (d) compares the petrologically and seismically derived temperature estimates (markers colored by physiographic province). Isotherms represent absolute temperature differences, i.e., $T_{pot}(seismology) - T_{pot}(petrology)$ (color coded and labeled).

that increasing Fe^{3+} in olivine results in increased dissipation of the shear modulus (Cline II et al., 2018), such that more oxidized/water-rich mantle appears seismically slower (and therefore hotter). Other regions show smaller differences (0°C to 100°C) and pertain to largely anhydrous tholeiitic provinces (Snake River Plain, Southern Nevada, and New Mexico) formed by decompression melting of upwelling asthenosphere (Fitton et al., 1991; Feuerbach et al., 1993; Leeman et al., 2009). This agreement therefore empirically verifies the accuracy of the seismic inversion in quantifying the thermochemical characteristics of more typical upper mantle.

The strength of this comparison lies in that surficial expressions of thermal anomalies may be linked to deep mantle structures. It also highlights the sensitivity of seismologically derived temperature-depth estimates to the specific petrological characteristics of the mantle, which changes with tectonic setting. Correctly accounting for these variations could help solve ambiguity in the chemical and isotopic signatures of eruptive provinces by imaging the thermal state of the underlying mantle in more detailed seismic and petrological surveys in the future.

8. Summary and Conclusions

In this paper, we proposed a methodology for processing, modeling, and inversion of multifrequency Ps and Sp converted body waves (RFs) and applied it to data recorded by USArray to perform a tomographic study of crust and mantle beneath the North American continent.

Careful data selection and processing has been found to be a central step in the construction of Sp RFs, since these are typically prone to be noisy and sense distinct mantle regions depending on source-receiver configuration. To properly account for this, we binned data into different back-azimuth bins and considered these separately. To further increase the robustness of our Sp RF stacks, we augmented the latter by combining data from USArray reference and transportable stations. Ultimately, only high-quality Ps and Sp RFs with clear conversions at the Moho, lithosphere, 410, and 660 were retained for inversion. Finally, to ensure consistency between observed and synthetic RF waveform amplitudes, processing of modeled waveforms mimicked that applied to real data in detail. As part of waveform verification, we also conducted a validation of our approach to computing synthetic waveforms in 1-D models by comparing these to full waveform synthetics computed in a 3-D velocity model.

Relying on a thermodynamic formulation, the forward model consisted of first computing seismic velocity and density models via Gibbs free energy minimization, followed by seismic waveform modeling to construct maps of the crust and thermochemical mantle structure underneath the contiguous United States. We were able to identify three major tectonic regions based on similarities in radial temperature and *S* wave velocity structure:

1. The TAW, comprising regions west of the Rocky Mountains, is characterized compositionally as more fertile (Mg# ~ 0.90), physically by a thinner lithosphere (100 ± 23 km), and thermally by higher mantle potential temperatures ($1490 \pm 27°$C). Consequently, shallow upper mantle *S* wave velocity is strongly diminished (by up to -5%), shear attenuation is increased, and the 410-km seismic discontinuity is shifted to greater depths (424 ± 7 km).
2. The COE, including most of the continent to the east of the Great Plains, is compositionally more depleted (Mg# ~ 0.91) and colder ($1413 \pm 27°$C), underlain by an overall thicker lithosphere (208 ± 33 km). Accordingly, *S* wave velocity is higher (by up to $+5\%$), shear attenuation is decreased, and the 410 appears at shallower depths (416 ± 6 km).
3. The CTR represents the tectonic region with intermediate properties in-between those of TAW and COE.

Despite being able to image well-known mantle features such as traces of active and ancient subduction or the Yellowstone plume, we note that resolving the exact shape and extent of such 3-D volumetric features by our method is limited by two factors: (1) we do not solve the inverse problem in a fully 3-D framework, but rather use a 1-D formulation to build a 3-D model a posteriori, and (2) converted waves are not directly sensitive to volumetric velocity changes, but rather to velocity contrasts across discontinuities. Further limitations of our method arise from the use of isentropes in modeling mantle thermal structure, the basalt-harzburgite compositional model, and the assumption of an equilibrium assemblage configuration. Further, the absence of thermodynamic data, for now, involving melt- and water-bearing systems might bias our results in certain regions, such as underneath the Cascades arc, as evidenced in the apparent mismatch with petrological estimates. Yet in spite of these limitations, a fully equilibrated, compositionally uniform, adiabatic, and dry mantle nevertheless provides an excellent fit to the observed seismic data. Our combination of geophysically derived potential temperature and lithospheric thickness estimates to those obtained from thermobarometric inversions of volcanic rock chemistry in the western United States show first-order agreement, permitting the assessment of broad-scale mantle melting conditions and their magmatic expression. This integrated approach represents a promising avenue for providing multidimensional insight into crustal tectonic structures and regimes and their link with deep mantle processes.

Data Availability Statement

The facilities of Incorporated Research Institutions for Seismology (IRIS) Data Services, and specifically the IRIS Data Management Center, were used for access to waveforms and related metadata. IRIS Data Services are funded through the Seismological Facilities for the Advancement of Geoscience (SAGE) Award of the National Science Foundation under Cooperative Support Agreement EAR-1851048. Data from the transportable array network were made freely available as part of the EarthScope USArray facility, operated by IRIS and supported by the National Science Foundation, under Cooperative Agreements EAR-1261681. Seismic data were downloaded via ObspyDMT (Hosseini & Sigloch, 2017) and processed using Obspy (Krischer et al., 2015) and the Python-package "rf" (Eulenfeld, 2020). Perple_X is available on www.perplex.ethz.ch, and we use the CMAES-implementation by N. Hansen et al. (2019). Maps were created by means of the Basemap Matplotlib Toolkit (matplotlib.org/basemap/). Tomographic mantle models SL2013NA, US-SL-2014, and GyPSuM were downloaded from IRIS-EMC (ds.iris.edu/ds/products/emc/), while model S362ANI and related codes are available on www.ldeo.columbia.edu/ekstrom/Projects/3D/BK/models.html.

Acknowledgments

We thank the editor, M. Bostock, for editorial handling and the associate editor V. Lekić, H. Yuan, and an anonymous reviewer for valuable comments that helped to improve the quality of the manuscript. This study is supported by a grant from the Swiss Federal Institute of Technology (ETH, project number ETH05 17-1). B.T. has received funding from the European Union's Horizon 2020 research and innovation program under the Marie Sklodowska-Curie grant agreement No. 793824. P.A.S. acknowledges support from the Swiss National Science Foundation via an Ambizione Fellowship (No. 180025). F.D.M. is supported by the Swiss National Science Foundation (Project No. 159907 and 191892). Computations were performed on the clusters Euler (ETH) and Piz Daint (CSCS). Computations on Piz Daint were supported by the Swiss National Supercomputing Centre (CSCS) under Project ID s922. Finally, we are grateful to M. Afanasiev, M. van Driel, S. Thrastarsson, L. Krischer, and W. Halter for support in simulating 3-D waveforms using the Salvus software package (www.mondaic.com).

References

Abt, D. L., Fischer, K. M., French, S. W., Ford, H. A., Yuan, H., & Romanowicz, B. (2010). North American lithospheric discontinuity structure imaged by Ps and Sp receiver functions. *Journal of Geophysical Research*, *115*, B09301. https://doi.org/10.1029/2009JB006914

Afanasiev, M., Boehm, C., van Driel, M., Krischer, L., Rietmann, M., May, D. A., et al. (2019). Modular and flexible spectral-element waveform modelling in two and three dimensions. *Geophysical Journal International*, *216*(3), 1675–1692. https://doi.org/10.1093/gji/ggy469

Afonso, J. C., Rawlinson, N., Yang, Y., Schutt, D. L., Jones, A. G., Fullea, J., & Griffin, W. L. (2016). 3D multiobservable probabilistic inversion for the compositional and thermal structure of the lithosphere and upper mantle: III. Thermochemical tomography in the Western Central U.S. *Journal of Geophysical Research*, *121*, 7337–7370. https://doi.org/10.1002/2016JB013049

Amante, C., & Eakins, B. W. (2009). Etopo1 1 arc-minute global relief model: Procedures, data sources and analysis. NOAA Technical Memorandum NESDIS NGDC-24. National Geophysical Data Center, NOAA.

Andrews, J., & Deuss, A. (2008). Detailed nature of the 660 km region of the mantle from global receiver function data. *Journal of Geophysical Research*, *113*, B06304. https://doi.org/10.1029/2007JB005111

Artemieva, I. M., & Mooney, W. D. (2001). Thermal thickness and evolution of Precambrian lithosphere: A global study. *Journal of Geophysical Research*, *106*(B6), 16,387–16,414. https://doi.org/10.1029/2000JB900439

Bagheri, A., Khan, A., Al-Attar, D., Crawford, O., & Giardini, D. (2019). Tidal response of Mars constrained from laboratory-based viscoelastic dissipation models and geophysical data. *Journal of Geophysical Research: Planets*, *124*, 2703–2727. https://doi.org/10.1029/2019JE006015

Becker, T. W. (2012). On recent seismic tomography for the western United States. *Geochemistry, Geophysics, Geosystems*, *13*, Q01W10. https://doi.org/10.1029/2011GC003977

Bensen, G. D., Ritzwoller, M. H., & Yang, Y. (2009). A 3-D shear velocity model of the crust and uppermost mantle beneath the United States from ambient seismic noise. *Geophysical Journal International*, *177*, 1177–1196. https://doi.org/10.1111/j.1365-246X.2009.04125.x

Bercovici, D., & Karato, S.-I. (2003). Whole-mantle convection and the transition-zone water filter. *Nature*, *425*(6953), 39–44.

Bina, C. R., & Helffrich, G. (1994). Phase transition Clapeyron slopes and transition zone seismic discontinuity topography. *Journal of Geophysical Research*, *99*(B8), 15,853–15,860. https://doi.org/10.1029/94JB00462

Bock, G. (1994). Multiples as precursors to S, SKS and ScS. *Geophysical Journal International*, *119*, 421–427.

Boyce, A., Bastow, I. D., Golos, E. M., Rondenay, S., Burdick, S., & van der Hilst, R. (2019). Variable modification of continental lithosphere during the Proterozoic Grenville orogeny: Evidence from teleseismic P-wave tomography. *Earth and Planetary Science Letters*, *525*, 115763. https://doi.org/10.1016/j.epsl.2019.115763

Buehler, J. S., & Shearer, P. M. (2017). Uppermost mantle seismic velocity structure beneath USArray. *Journal of Geophysical Research: Solid Earth*, *122*, 436–448. https://doi.org/10.1002/2016JB013265

Burdick, S., Li, C., Martynov, V., Cox, T., Eakins, J., Mulder, T., et al. (2008). Upper mantle heterogeneity beneath North America from travel time tomography with global and USArray transportable array data. *Seismological Research Letters*, *79*(3), 384–392. https://doi.org/10.1785/gssrl.79.3.384

Burdick, S., van der Hilst, R. D., Vernon, F. L., Martynov, V., Cox, T., Eakins, J., et al. (2010). Model update January 2010: Upper mantle heterogeneity beneath North America from traveltime tomography with global and USArray transportable array data. *Seismological Research Letters*, *81*(5), 689–693. https://doi.org/10.1785/gssrl.81.5.689

Calò, M., Bodin, T., & Romanowicz, B. (2016). Layered structure in the upper mantle across North America from joint inversion of long and short period seismic data. *Earth and Planetary Science Letters*, *449*, 164–175. https://doi.org/10.1016/j.epsl.2016.05.054

Cao, A., & Lavender, A. (2010). High-resolution transition zone structures of the Goreda Slab beneath the western United States: Implication for deepwater subduction. *Journal of Geophysical Research*, *115*, B07301. https://doi.org/10.1029/2009JB006876

Chen, C., Zhao, D., & Wu, S. (2014). Crust and upper mantle structure of the New Madrid Seismic Zone: Insight into intraplate earthquakes. *Physics of the Earth and Planetary Interiors*, *230*, 1–14. https://doi.org/10.1016/j.pepi.2014.01.016

Chen, C., Zhao, D., & Wu, S. (2015). Tomographic imaging of the Cascadia subduction zone: Constraints on the Juan de Fuca slab. *Tectonophysics*, *648*, 73–88. https://doi.org/10.1016/j.tecto.2015.02.012

Chen, L. (2009). Lithospheric structure variations between the eastern and central North China Craton from S- and P-receiver function migration. *Physics of the Earth and Planetary Interiors*, *173*, 216–227. https://doi.org/10.1016/j.pepi.2008.11.011

Clark, A. N., & Lesher, C. E. (2017). Elastic properties of silicate melts: Implications for low velocity zones at the lithosphere-asthenosphere boundary. *Science Advances*, *3*(12), 1–5. https://doi.org/10.1126/sciadv.1701312

Cline II, C. J., Faul, U. H., David, E. C., Berry, A. J., & Jackson, I. (2018). Redox-influenced seismic properties of upper-mantle olivine. *Nature*, *555*(7696), 355–358. https://doi.org/10.1038/nature25764

Connolly, J. A. D. (2009). The geodynamic equation of state: What and how. *Geochemistry, Geophysics, Geosystems*, *10*, Q10014. https://doi.org/10.1029/2009GC002540

Connolly, J. A. D., & Khan, A. (2016). Uncertainty of mantle geophysical properties computed from phase equilibrium models. *Geophysical Research Letters*, *43*, 5026–5034. https://doi.org/10.1002/2016GL068239

Cottaar, S., & Deuss, A. (2016). Large-scale mantle discontinuity topography beneath Europe: Signature of akimotoite in subducting slabs. *Journal of Geophysical Research: Solid Earth*, *121*, 279–292. https://doi.org/10.1002/2015JB012452

Crotwell, H. P., Owens, T. J., & Ritsema, J. (1999). The TauP Toolkit: Flexible seismic travel-time and ray-path utilities. *Seismological Research Letters*, *70*, 154–160. https://doi.org/10.1785/gssrl.70.2.154

Dickinson, W. R. (2004). Evolution of the North American Cordillera. *Annual Review of Earth and Planetary Science*, *32*, 13–45. https://doi.org/10.1146/annurev.earth.32.101802.120257

Dueker, K. G., & Sheehan, A. F. (1997). Mantle discontinuity structure from midpoint stacks of converted P to S waves across the Yellowstone hotspot track. *Journal of Geophysical Research*, *102*(B4), 8313–8327. https://doi.org/10.1029/96JB03857

Dziewonski, A. M., & Anderson, D. L. (1981). Preliminary reference Earth model. *Physics of the Earth and Planetary Interiors*, *25*, 297–356. https://doi.org/10.1016/0031-9201(81)90046-7

Dziewonski, A. M., Chou, T.-A., & Woodhouse, J. H. (1981). Determination of earthquake source parameters from waveform data for studies of global and regional seismicity. *Journal of Geophysical Research*, *86*(B4), 2825–2852. https://doi.org/10.1029/JB086iB04p02825

Eaton, D. W., Darbyshire, F., Evans, R. L., Grütter, H., Jones, A. G., & Yuan, X. (2009). The elusive lithosphere-asthenosphere boundary (LAB) beneath cratons. *Lithos*, *109*(1–2), 1–22. https://doi.org/10.1016/j.lithos.2008.05.009

Efron, B., & Tibshirani, R. (1991). Statistical data analysis in the computer age. *Science*, *253*(5018), 390–395. https://doi.org/10.1126/science.253.5018.390

Eilon, Z., Fischer, K. M., & Dalton, C. A. (2018). An adaptive Bayesian inversion for upper-mantle structure using surface waves and scattered body waves. *Geophysical Journal International*, *214*, 232–253. https://doi.org/10.1093/gji/ggy137

Ekström, G., Nettles, M., & Dziewonski, A. M. (2012). The global CMT project 2004-2010: Centroid-moment tensors for 13,017 earthquakes. *Physics of the Earth and Planetary Interiors*, *200–201*, 1–9. https://doi.org/10.1016/j.pepi.2012.04.002

Eulenfeld, T. (2020). Rf: Receiver function calculation in seismology. *Journal of Open Source Software*, *5*(48), 1808. https://doi.org/10.21105/joss.01808

Farra, V., & Vinnik, L. (2000). Upper mantle stratification by P and S receiver functions. *Geophysical Journal International*, *141*(3), 699–712. https://doi.org/10.1046/j.1365-246x.2000.00118.x

Fenneman, N. M. (1928). Physiographic divisions of the United States. *Annals of the Association of American Geographers*, *18*(4), 261–353.

Férot, A., & Bolfan-Casanova, N. (2012). Water storage capacity in olivine and pyroxene to 14 GPa: Implications for the water content of the Earth's upper mantle and nature of seismic discontinuities. *Earth and Planetary Science Letters*, *349–350*, 218–230. https://doi.org/10.1016/j.epsl.2012.06.022

Feuerbach, D. L., Smith, E., Walker, J. D., & Tangeman, J. A. (1993). The role of the mantle during crustal extension: Constraints from geochemistry of volcanic rocks in the Lake Mead area, Nevada and Arizona. *Geological Society of America Bulletin*, *105*(12), 1561–1575. https://doi.org/10.1130/0016-7606(1993)105<1561:TROTMD>2.3.CO;2

Fitton, J. G., James, D., & Leeman, W. P. (1991). Basic magmatism associated with Late Cenozoic extension in the compositional variations in space and time. *Journal of Geophysical Research*, *96*(B8), 13,693–13,711. https://doi.org/10.1029/91JB00372

Flanagan, M. P., & Shearer, P. M. (1998). Global mapping of topography on transition zone velocity discontinuities by stacking SS precursors. *Journal of Geophysical Research*, *103*(B2), 2673–2692. https://doi.org/10.1029/97JB03212

Ford, H. A., Fischer, K. M., Abt, D. L., Rychert, C. A., & Elkins-Tanton, L. T. (2010). The lithosphere asthenosphere boundary and cratonic lithospheric layering beneath Australia from Sp wave imaging. *Earth and Planetary Science Letters*, *300*(3), 299–310. https://doi.org/10.1016/j.epsl.2010.10.007

Freitas, D., Mathilake, G., Schiavi, F., Chantel, J., Bolfan-Casanova, N., Bouhifd, M. A., & Andrault, D. (2017). Experimental evidence supporting a global melt layer at the base of the Earth's upper mantle. *Nature Communications*, *8*, 2186. https://doi.org/10.1038/s41467-017-02275-9

Fuchs, K., & Müller, G. (1971). Computation of synthetic seismograms with the reflectivity method and comparison with observations. *Geophysical Journal International*, *23*(4), 417–433. https://doi.org/10.1111/j.1365-246X.1971.tb01834.x

Gao, S. S., & Liu, K. H. (2014). Mantle transition zone discontinuities beneath the contiguous United States. *Journal of Geophysical Research: Solid Earth*, *119*, 6452–6468. https://doi.org/10.1002/2014JB011253

Geissler, W. H., Sodoudi, F., & Kind, R. (2010). Thickness of the central and eastern European lithosphere as seen by S receiver functions. *Geophysical Journal International*, *181*(2), 604–634. https://doi.org/10.1111/j.1365-246X.2010.04548.x

Grand, S. P., & Helmberger, D. V. (1984). Upper mantle shear structure of North America. *Geophysical Journal International*, *76*(2), 399–438. https://doi.org/10.1111/j.1365-246X.1984.tb05053.x

Green, D. H., Hibberson, W. O., Kovács, I., & Rosenthal, A. (2010). Water and its influence on the lithosphere–asthenosphere boundary. *Nature*, *467*, 448–451. https://doi.org/10.1038/nature09369

Grove, T. L., Parman, S. W., Bowring, S. A., Price, R. C., & Baker, M. B. (2002). The role of an H_2O-rich fluid component in the generation of primitive basaltic andesites and andesites from the Mt. Shasta region, N California. *Contributions to Mineralogy and Petrology*, *142*, 375–396. https://doi.org/10.1007/s004100100299

Hansen, N., Akimoto, Y., & Baudis, P. (2019). CMA-ES/pycma on Github. Zenodo, https://doi.org/10.5281/zenodo.2559634

Hansen, N., & Ostermeier, A. (2001). Completely derandomized self-adaptation in evolution strategies. *Evolutionary Computation*, *9*(2), 159–195. https://doi.org/10.1162/106365601750190398

Hansen, S. M., Dueker, K., & Schmandt, B. (2015). Thermal classification of lithospheric discontinuities beneath USArray. *Earth and Planetary Science Letters*, *431*, 36–47. https://doi.org/10.1016/j.epsl.2015.09.009

Hastings, W. K. (1970). Monte Carlo sampling methods using Markov chains and their applications. *Biometrika*, *57*(1), 97–109. https://doi.org/10.2307/2334940

Heit, B., Sodoudi, F., Yuan, X., Bianchi, M., & Kind, R. (2007). An S receiver function analysis of the lithospheric structure in South America. *Geophysical Research Letters*, *34*, L14307. https://doi.org/10.1029/2007GL030317

Helffrich, G. (2000). Topography of the transition zone discontinuities. *Reviews of Geophysics*, *38*(1), 141–158. https://doi.org/10.1029/1999RG000060

Helffrich, G. R., & Wood, B. J. (2001). The Earth's mantle. *Nature*, *412*(6613), 219–229. https://doi.org/10.1038/35087500

Hill, R. (1952). The elastic behaviour of a crystalline aggregate. *Proceedings of the Physical Society. Section A*, *65*, 349–354. https://doi.org/10.1088/03701298/65/5/307

Hirose, K. (2002). Phase transitions in pyrolitic mantle around 670-km depth: Implications for upwelling of plumes from the lower mantle. *Journal of Geophysical Research*, *107*(B4), ECV 3–1-ECV 3-13.

Hirschmann, M. M. (2006). Water, melting, and the deep earth H_2O cycle. *Annual Review of Earth and Planetary Science*, *34*, 629–653. https://doi.org/10.1146/annurev.earth.34.031405.125211

Hoffman, P. F. (1988). United plates of America, the birth of a craton: Early Proterozoic assembly and growth of Laurentia. *Annual Review of Earth and Planetary Science*, *16*, 543–603. https://doi.org/10.1146/annurev.ea.16.050188.002551

Hoffman, P. F. (1989). Precambrian geology and tectonic history of North America. In A. W. Bally, & A. R. Palmer (Eds.), *The geology of North America—An overview, vol. A*. Boulder, CO: The Geological Society of America.

Hopper, E., Ford, H. A., Fischer, K. M., Lekić, V., & Fouch, M. J. (2014). The lithosphere asthenosphere boundary and the tectonic and magmatic history of the northwestern United States. *Earth and Planetary Science Letters*, *402*, 69–81. https://doi.org/10.1016/j.epsl.2013.12.016

Hosseini, K., & Sigloch, K. (2017). ObspyDMT: A Python toolbox for retrieving and processing large seismological data sets. *Solid Earth*, *8*, 1047–1070. https://doi.org/10.5194/se-8-1047-2017

Houser, C., Masters, G., Shearer, P., & Laske, G. (2008). Shear and compressional velocity models of the mantle from cluster analysis of long-period waveforms. *Geophysical Journal International*, *174*, 195–212. https://doi.org/10.1111/j.1365-246X.2008.03763.x

Humphreys, E. (2009). Relation of flat subduction to magmatism and deformation in the western United States. Backbone of the Americas: Shallow Subduction, Plateau Uplift, and Ridge and Terrane Collision, Geological Society of America.

Jackson, I., & Faul, U. H. (2010). Grainsize-sensitive viscoelastic relaxation in olivine: Towards a robust laboratory-based model for seismological application. *Physics of the Earth and Planetary Interiors*, *183*(1–2), 151–163. https://doi.org/10.1016/j.pepi.2010.09.005

James, D. E., Fouch, M. J., Carlson, R. W., & Roth, J. B. (2011). Slab fragmentation, edge flow and the origin of the Yellowstone hotspot track. *Earth and Planetary Science Letters*, *311*(1-2), 124–135. https://doi.org/10.1016/j.epsl.2011.09.007

Jaupart, C., & Mareschal, J.-C. (1999). Thermal structure and thickness of continental roots. *Lithos*, *48*, 93–114. https://doi.org/10.1016/S0419-0254(99)80007-X

Karato, S., Olugboji, T., & Park, J. (2015). Mechanisms and geologic significance of the mid-lithosphere discontinuity in the continents. *Nature Geoscience*, *8*, 509–514. https://doi.org/10.1038/NGEO2462

Karato, S., & Park, J. (2019). On the origin of the upper mantle seismic discontinuities. In H. Yuan & B. Romanowicz (Eds.), *Lithospheric discontinuities*. Washington, DC: American Geophysical Union.

Kawakatsu, H., Kumar, P., Takei, Y., Shinohara, M., Kanazawa, T., Araki, E., & Suyehiro, K.(2009). Seismic evidence for sharp lithosphere-asthenosphere boundaries of oceanic plates. *Science*, *324*(5926), 499–502. https://doi.org/10.1126/science.1169499

Kennett, B. L. N., & Engdahl, E. R. (1991). Traveltimes for global earthquake location and phase identification. *Geophysical Journal International*, *105*, 429–465. https://doi.org/10.1111/j.1365-246X.1991.tb06724.x

Khan, A., Boschi, L., & Connolly, J. A. D. (2009). On mantle chemical and thermal heterogeneities and anisotropy as mapped by inversion of global surface wave data. *Journal of Geophysical Research*, *114*, B09305. https://doi.org/10.1029/2009JB006399

Khan, A., & Shankland, T. J. (2012). A geophysical perspective on mantle water content and melting: Inverting electromagnetic sounding data using laboratory-based electrical conductivity profiles. *Earth and Planetary Science Letters*, *317-318*, 27–43. https://doi.org/10.1016/j.epsl.2011.11.031

Khan, A., Zunino, A., & Deschamps, F. (2011). The thermo chemical and physical structure beneath the North American continent from Bayesian inversion of surface wave phase velocities. *Journal of Geophysical Research*, *116*, B09304. https://doi.org/10.1029/2011JB008380

Kind, R., Mooney, W. D., & Yuan, X. (2020). New insights into the structural elements of the upper mantle beneath the contiguous United States from S-to-P converted seismic waves. *Geophysical Journal International*, *222*, 646–659. https://doi.org/10.1093/gji/ggaa203

Kind, R., Yuan, X., & Kumar, P. (2012). Seismic receiver functions and the lithosphere asthenosphere boundary. *Tectonophysics*, *536-537*, 25–43. https://doi.org/10.1016/j.tecto.2012.03.005

Kind, R., Yuan, X., Mechie, J., & Sodoudi, F. (2015). Structure of the upper mantle in the north-western and central United States from USArray S-receiver functions. *Solid Earth*, *6*, 957–970. https://doi.org/10.5194/se-6-957-2015

Knapmeyer-Endrun, B., Krüger, F., Geissler, W. H., & PASSEQ Working Group (2017). Upper mantle structure across the Trans-European Suture Zone imaged by S-receiver functions. *Earth and Planetary Science Letters*, *458*, 429–441. https://doi.org/10.1016/j.epsl.2016.11.011

Kohlstedt, D., Keppler, H., & Rubie, D. (1996). Solubility of water in the α, β and γ phases of $(Mg,Fe)_2SiO_4$. *Contributions to Mineralogy and Petrology*, *123*, 345–357. https://doi.org/10.1007/s004100050161

Kosarev, G., Kind, R., Sobolev, S. V., Yuan, X., Hanka, W., & Oreshin, S. (1999). Seismic evidence for a detached Indian lithospheric mantle beneath Tibet. *Science*, *283*(5406), 1306–1309. https://doi.org/10.1126/science.283.5406.1306

Krischer, L., Fichtner, A., Boehm, C., & Igel, H. (2018). Automated large-scale full seismic waveform inversion for North America and the North Atlantic. *Journal of Geophysical Research: Solid Earth*, *123*, 5902–5928. https://doi.org/10.1029/2017JB015289

Krischer, L., Megies, T., Barsch, R., Beyreuther, M., Lecocq, T., Caudron, C., & Wassermann, J. (2015). ObsPy: A bridge for seismology into the scientific Python ecosystem. *Computational Science & Discovery*, *8*(1), 014003. https://doi.org/10.1088/1749-4699/8/1/014003

Kumar, P., Yuan, X., Kind, R., & Kosarev, G. (2005). The lithosphere-asthenosphere boundary in the Tien Shan-Karakoram region from S receiver functions: Evidence for continental subduction. *Geophysical Research Letters*, *32*, L07305. https://doi.org/10.1029/2004GL022291

Langston, C. A. (1979). Structure under Mount Rainier, Washington, inferred from teleseismic body waves. *Journal of Geophysical Research*, *84*(B9), 4749–4762. https://doi.org/10.1029/JB084iB09p04749

Laske, G., Masters, G., Ma, Z., & Pasyanos, M. (2013). Update on CRUST1.0—A 1-degree Global Model of Earth's Crust. Geophys. Res. Abstracts, 15, Abstract EGU2013-2658.

Lawrence, J. F., & Shearer, P. M. (2006). A global study of transition zone thickness using receiver functions. *Journal of Geophysical Research*, *111*, B06307. https://doi.org/10.1029/2005JB003973

Lee, C.-T. A., Luffi, P., Plank, T., Dalton, H., & Leeman, W. P. (2009). Constraints on the depths and temperatures of basaltic magma generation on Earth and other terrestrial planets using new thermobarometers for mafic magmas. *Earth and Planetary Science Letters*, *279*(1-2), 20–33. https://doi.org/10.1016/j.epsl.2008.12.020

Leeman, W. P., Lewis, J. F., Evarts, R. C., Conrey, R. M., & Streck, M. J. (2005). Petrologic constraints on the thermal structure of the Cascades arc. *Journal of Volcanology and Geothermal Research*, *140*(1–3), 67–105. https://doi.org/10.1016/j.jvolgeores.2004.07.016

Leeman, W. P., Schutt, D. L., & Hughes, S. S. (2009). Thermal structure beneath the Snake River Plain: Implications for the Yellowstone hotspot. *Journal of Volcanology and Geothermal Research*, *188*(1–3), 57–67. https://doi.org/10.1016/j.jvolgeores.2009.01.034

Lekić, V., Cottaar, S., Dziewonski, A., & Romanowicz, B. (2012). Cluster analysis of global lower mantle tomography: A new class of structure and implications for chemical heterogeneity. *Earth and Planetary Science Letters*, *357–358*, 68–77. https://doi.org/10.1016/j.epsl.2012.09.014

Lekić, V., & Fischer, K. M. (2014). Contrasting lithospheric signatures across the western United States revealed by Sp receiver functions. *Earth and Planetary Science Letters*, *402*, 90–98. https://doi.org/10.1016/j.epsl.2013.11.026

Lekić, V., & Fischer, K. M. (2017). Interpreting spatially stacked Sp receiver functions. *Geophysical Journal International*, *210*(2), 874–886. https://doi.org/10.1093/gji/ggx206

Lekić, V., French, S. W., & Fischer, K. M. (2011). Lithospheric thinning beneath rifted regions of Southern California. *Science*, *334*, 783–787. https://doi.org/10.1126/science.1208898

Lekić, V., & Romanowicz, B. (2011). Tectonic regionalization without a priori information: A cluster analysis of upper mantle tomography. *Earth and Planetary Science Letters*, *308*, 151–160. https://doi.org/10.1016/j.epsl.2011.05.050

Levander, A., & Miller, M. S. (2012). Evolutionary aspects of lithosphere discontinuity structure in the western U.S. *Geochemistry, Geophysics, Geosystems*, *13*, Q0AK07. https://doi.org/10.1029/2012GC004056

Li, X., Yuan, X., & Kind, R. (2007). The lithosphere–asthenosphere boundary beneath the western United States. *Geophysical Journal International*, *170*, 700–710. https://doi.org/10.1111/j.1365-246X.2007.03428.x

Ligorría, J. P., & Ammon, C. J. (1999). Iterative deconvolution and receiver-function estimation. *Bulletin of the Seismological Society of America*, *89*(5), 1395–1400.

Liu, H., Wang, W., Jia, X., Leng, W., Zhongqing, W., & Sun, D. (2018). The combined effects of post-spinel and post-garnet phase transitions on mantle plume dynamics. *Earth and Planetary Science Letters*, *496*, 80–88. https://doi.org/10.1016/j.epsl.2018.05.031

Liu, K. H. (2003). Effects of inelasticity on the apparent depth and detectability of seismic discontinuities in the mantle. *Geophysical Research Letters*, *30*(9), 1455. https://doi.org/10.1029/2002GL015264

Lowry, A. R., & Peréz-Gussinyé, M. (2011). The role of crustal quartz in controlling Cordilleran deformation. *Nature*, *471*, 353–357. https://doi.org/10.1038/nature09912

Ma, X., & Lowry, A. R. (2017). USArray imaging of continental crust in the conterminous United States. *Tectonics*, *36*, 2882–2902. https://doi.org/10.1002/2017TC004540

MacQueen, J. B. (1967). Some methods for classification and analysis of multivariate observations. In *Proceedings of 5th Berkeley Symposium on Mathematical Statistics and Probability. Band 1*: University of California Press (pp. 281–297).

Maguire, R., Ritsema, J., & Goes, S. (2018). Evidence of subduction-related thermal and compositional heterogeneity below the United States from transition zone receiver functions. *Geophysical Research Letters*, *45*, 8913–8922. https://doi.org/10.1029/2018GL078378

Makushkina, A., Tauzin, B., Tkalčić, H., & Thybo, H. (2019). The mantle transition zone in Fennoscandia: Enigmatic high topography without deep mantle thermal anomaly. *Geophysical Research Letters*, *46*, 3652–3662. https://doi.org/10.1029/2018GL081742

McKenzie, D., & Bickle, M. (1988). The volume and composition of melt generated by extension of the lithosphere. *Journal of Petrology*, *29*(3), 625–679. https://doi.org/10.1093/petrology/29.3.625

Metropolis, N., Rosenbluth, A. W., Rosenbluth, M. N., Teller, A. H., & Teller, E. (1953). Equation of state calculations by fast computing machines. *The Journal of Chemical Physics*, *21*(6), 1087–1092. https://doi.org/10.1063/1.1699114

Miller, M. S., & Eaton, D. W. (2010). Formation of cratonic mantle keels by arc accretion: Evidence from S receiver functions. *Geophysical Research Letters*, *37*, L18305. https://doi.org/10.1029/2010GL044366

Monna, S., Montuori, C., Piromallo, C., & Vinnik, L. (2019). Mantle structure in the central mediterranean region from P and S receiver functions. *Geochemistry, Geophysics, Geosystems*, *20*, 4545–4566. https://doi.org/10.1029/2019GC008496

Mooney, W. D., & Kaban, M. K. (2010). The North American upper mantle: Density, composition, and evolution. *Journal of Geophysical Research*, *115*, B12424. https://doi.org/10.1029/2010JB000866

Mosegaard, K., & Tarantola, A. (1995). Monte Carlo sampling of solutions to inverse problems. *Journal of Geophysical Research*, *100*(B7), 12,431–12,447. https://doi.org/10.1029/94JB03097

Mosegaard, K., & Tarantola, A. (2002). Probabilistic approach to inverse problems. In *International handbook of earthquake and engineering seismology* (pp. 237–265). Academic Press.

Müller, G. (1985). The reflectivity method: A tutorial. *Journal of Geophysical Research*, *58*, 153–174.

Munch, F. D., Khan, A., Tauzin, B., van Driel, M., & Giardini, D. (2020). Seismological evidence for thermo-chemical heterogeneity in Earth's continental mantle. *Earth and Planetary Science Letters*, *539*, 1–9. https://doi.org/10.1016/j.epsl.2020.116240

Munch, F. D., Khan, A., Tauzin, B., Zunino, A., & Giardini, D. (2018). Stochastic inversion of P to S converted waves for mantle thermal and compositional structure: Methodology and application. *Journal of Geophysical Research: Solid Earth*, *123*, 10,706–10,726. https://doi.org/10.1029/2018JB016032

Nelson, P. L., & Grand, S. P. (2018). Lower-mantle plume beneath the Yellowstone hotspot revealed by core waves. *Nature Geoscience*, *11*, 280–284. https://doi.org/10.1038/s41561-018-0075-y

Nettles, M., & Dziewonski, A. (2008). Radially anisotropic shear velocity structure of the upper mantle globally and beneath North America. *Journal of Geophysical Research*, *113*, B02303. https://doi.org/10.1029/2006JB004819

Obrebski, M., Allen, R. M., Pollitz, F., & Hung, S.-H. (2011). Lithosphere-asthenosphere interaction beneath the western United States from the joint inversion of body-wave travel-times and surface-wave phase velocities. *Geophysical Journal International*, *185*(2), 1003–1021. https://doi.org/10.1111/j.1365-246X.2011.04990.x

Obrebski, M., Allen, R. M., Xue, M., & Hung, S.-H. (2010). Slab-plume interaction beneath the Pacific Northwest. *Geophysical Research Letters*, *37*, L14305. https://doi.org/10.1029/2010GL043489

Plank, T., & Forsyth, D. W. (2016). Thermal structure and melting conditions in the mantle beneath the Basin and Range province from seismology and petrology. *Geochemistry, Geophysics, Geosystems*, *17*, 1312–1338. https://doi.org/10.1002/2015GC006205

Porritt, R. W., Allen, R. M., & Pollitz, F. F. (2014). Seismic imaging east of the Rocky Mountains with USArray. *Earth and Planetary Science Letters*, *402*, 16–25. https://doi.org/10.1016/j.epsl.2013.10.034

Portner, D. E., & Hayes, G. P. (2018). Incorporating teleseismic tomography data into models of upper mantle slab geometry. *Geophysical Journal International*, *215*(1), 325–332. https://doi.org/10.1093/gji/ggy279

Rader, E., Emry, E., Schmerr, N., Frost, D., Cheng, C., Menard, J., et al. (2015). Characterization and petrological constraints of the midlithospheric discontinuity. *Geochemistry, Geophysics, Geosystems*, *16*, 3484–3504. https://doi.org/10.1002/2015GC005943

Ringwood, A. (1975). *Composition and petrology of the Earth's mantle*. New York: McGraw-Hill.

Rondenay, S. (2009). Upper mantle imaging with array recordings of converted and scattered teleseismic waves. *Surveys in Geophysics*, *30*, 377–405. https://doi.org/10.1007/s10712-009-9071-5

Roth, J. B., Fouch, M. J., James, D. E., & Carlson, R. W. (2008). Three dimensional seismic velocity structure of the northwestern United States. *Geophysical Research Letters*, *35*, L15304. https://doi.org/10.1029/2008GL034669

Rychert, C. A., Rondenay, S., & Fischer, K. M. (2007). P-to-S and S-to-P imaging of a sharp lithosphere asthenosphere boundary beneath eastern North America. *Journal of Geophysical Research*, *112*, B08314. https://doi.org/10.1029/2006JB004619

Rychert, C. A., & Shearer, P. M. (2009). A global view of the lithosphere-asthenosphere boundary. *Science*, *324*(5926), 495–498. https://doi.org/10.1126/science.1169754

Savage, B., & Silver, P. G. (2008). Evidence for a compositional boundary within the lithospheric mantle beneath the Kalahari craton from S receiver functions. *Earth and Planetary Science Letters*, *272*, 600–609. https://doi.org/10.1016/j.epsl.2008.05.026

Schaeffer, A., & Lebedev, S. (2014). Imaging the North American continent using waveform inversion of global and USArray data. *Earth and Planetary Science Letters*, *402*, 26–41. https://doi.org/10.1016/j.epsl.2014.05.014

Schmandt, B., & Humphreys, E. (2010). Complex subduction and small-scale convection revealed by body-wave tomography of the western United States upper mantle. *Earth and Planetary Science Letters*, *297*, 435–445. https://doi.org/10.1016/j.epsl.2010.06.047

Schmandt, B., & Humphreys, E. (2011). Seismically imaged relict slab from the 55 Ma Siletzia accretion to the northwest United States. *Geology*, *39*(2), 175–178. https://doi.org/10.1130/G31558.1

Schmandt, B., & Lin, F.-C. (2014). P and S wave tomography of the mantle beneath the United States. *Geophysical Research Letters*, *41*, 6342–6349. https://doi.org/10.1002/2014GL061231

Schmandt, B., Lin, F.-C., & Karlstrom, K. E. (2015). Distinct crustal isostasy trends east and west of the Rocky Mountain Front. *Geophysical Research Letters*, *42*, 10,290–10,298. https://doi.org/10.1002/2015GL066593

Schulze, K., Marquardt, H., Kawazoe, T., Ballaran, T. B., McCammon, C., Koch-Müller, M., et al. (2018). Seismically invisible water in Earth's transition zone? *Earth and Planetary Science Letters*, *498*, 9–16. https://doi.org/10.1016/j.epsl.2018.06.021

Selway, K., Ford, H., & Kelemen, P. (2015). The seismic mid-lithosphere discontinuity. *Earth and Planetary Science Letters*, *414*, 45–57. https://doi.org/10.1016/j.epsl.2014.12.029

Shen, W., & Ritzwoller, M. H. (2016). Crustal and uppermost mantle structure beneath the United States. *Journal of Geophysical Research: Solid Earth*, *121*, 4306–4342. https://doi.org/10.1002/2016JB012887

Shen, X., Kim, Y., Song, T.-R. A., & Lim, H. (2019). Data-oriented constraint on the interpretation of S receiver function and its application to observations of seismic discontinuities in the lithosphere asthenosphere system. *Geophysical Journal International*, *219*, 496–513. https://doi.org/10.1016/j.epsl.2018.05.031

Sigloch, K. (2011). Mantle provinces under North America from multifrequency P wave tomography. *Geochemistry, Geophysics, Geosystems*, *12*, Q02W08. https://doi.org/10.1029/2010GC003421

Smyth, J. R. (1987). β-Mg_2SiO_4: A potential host for water in the mantle? *American Mineralogist*, *72*, 1051–1055.

Sodoudi, F., Yuan, X., Kind, R., Lebedev, S., Adam, J. M. C., Kästle, E., & Tilmann, F. (2013). Seismic evidence for stratification in composition and anisotropic fabric within the thick lithosphere of Kalahari Craton. *Geochemistry, Geophysics, Geosystems*, *14*, 5393–5412. https://doi.org/10.1002/2013GC004955

Sodoudi, F., Yuan, X., Liu, Q., Kind, R., & Chen, J. (2006). Lithospheric thickness beneath the Dabie Shan, central eastern China from S receiver functions. *Geophysical Journal International*, *166*, 1363–1367. https://doi.org/10.1111/j.1365-246X.2006.03080.x

Sonder, L. J., & Jones, C. H. (1999). Western United States extension: How the West was widened. *Annual Review of Earth and Planetary Science*, *27*(1), 417–462. https://doi.org/10.1146/annurev.earth.27.1.417

Song, T.-R. A., Helmberger, D. V., & Grand, S. P. (2004). Low-velocity zone atop the 410-km seismic discontinuity in the northwestern United States. *Nature*, *427*, 530–533. https://doi.org/10.1038/nature02231

Spetzler, J., & Snieder, R. (2004). The Fresnel volume and transmitted waves. *Geophysics*, *69*(3), 653–663. https://doi.org/10.1190/1.1759451

Stein, S., Stein, C. A., Elling, R., Kley, J., Keller, G. R., Wysession, M., et al. (2015). Insights from North America's failed Midcontinent Rift into the evolution of continental rifts and passive continental margins. *Tectonophysics*, *744*, 403–421. https://doi.org/10.1016/j.tecto.2018.07.021

Stern, T. A., Henrys, S. A., Okaya, D., Louie, M. K., Savage, S., Lamb, H., et al. (2015). A seismic reflection image for the base of a tectonic plate. *Nature*, *518*, 85–88. https://doi.org/10.1038/nature14146

Stixrude, L., & Lithgow-Bertelloni, C. (2005). Thermodynamics of mantle minerals—I. Physical properties. *Geophysical Journal International*, *162*(2), 610–632. https://doi.org/10.1111/j.1365-246X.2005.02642.x

Stixrude, L., & Lithgow-Bertelloni, C. (2011). Thermodynamics of mantle minerals—II. Phase equilibria. *Geophysical Journal International*, *184*(3), 1180–1213. https://doi.org/10.1111/j.1365-246X.2010.04890.x

Sundberg, M., & Cooper, R. (2010). A composite viscoelastic model for incorporating grain boundary sliding and transient diffusion creep; correlating creep and attenuation responses for materials with a fine grain size. *Philosophical Magazine*, *90*(20), 2817–2840. https://doi.org/10.1080/14786431003746656

Tackley, P. J., Xie, S., Nakagawa, T., & Hernlund, J. W. (2005). Numerical and laboratory studies of mantle convection: Philosophy, accomplishments, and thermochemical structure and evolution. In R. D. van der Hilst, J. D. Bass, J. Matas, J. Trampert (Eds.), *Earth's deep mantle: Structure, composition, and evolution*. Washington, DC: American Geophysical Union.

Tan, Y., & Helmberger, D. V. (2007). Trans-Pacific upper mantle shear velocity structure. *Journal of Geophysical Research*, *112*, B08301. https://doi.org/10.1029/2006JB004853

Tauzin, B., Debayle, E., & Wittlinger, G. (2008). The mantle transition zone as seen by global Pds phases: No clear evidence for a thin transition zone beneath hotspots. *Journal of Geophysical Research*, *113*, B08309. https://doi.org/10.1029/2007JB005364

Tauzin, B., Debayle, E., & Wittlinger, G. (2010). Seismic evidence for a global low-velocity layer within the Earth's upper mantle. *Nature Geoscience*, *3*, 718–721. https://doi.org/10.1038/ngeo969

Tauzin, B., Kim, S., & Kennett, B. L. N. (2017). Pervasive seismic low-velocity zones within stagnant plates in the mantle transition zone: Thermal or compositional origin? *Earth and Planetary Science Letters*, *477*, 1–13. https://doi.org/10.1016/j.epsl.2017.08.006

Tauzin, B., van der Hilst, R. D., Wittlinger, G., & Ricard, Y. (2013). Multiple transition zone seismic discontinuities and low velocity layers below western United States. *Journal of Geophysical Research: Solid Earth*, *118*, 2307–2322. https://doi.org/10.1002/jgrb.50182

Thio, V., Cobden, L., & Trampert, J. (2015). Seismic signature of a hydrous mantle transition zone. *Physics of the Earth and Planetary Interiors*, *250*, 46–63. https://doi.org/10.1016/j.pepi.2015.11.005

Toffelmier, D. A., & Tyburczy, J. A. (2007). Electromagnetic detection of a 410-km-deep melt layer in the southwestern United States. *Nature*, *447*, 991–994. https://doi.org/10.1038/nature05922

van der Lee, S., & Frederiksen, A. (2005). Surface wave tomography applied to the North American upper mantle. In A. Levander & G. Nolet (Eds.), *Seismic Earth: Array analysis of broadband seismograms* (pp. 67–80). Washington, DC: AGU.

van der Lee, S., & Nolet, G. (1997). Seismic image of the subducted trailing fragments of the Farallon plate. *Nature*, *386*(6622), 266–269. https://doi.org/10.1038/386266a0

Vinnik, L., & Farra, V. (2007). Low S velocity atop the 410-km discontinuity and mantle plumes. *Earth and Planetary Science Letters*, *262*, 398–412. https://doi.org/10.1016/j.epsl.2007.07.051

Vinnik, L., Ren, Y., Stutzmann, E., Farra, V., & Kiselev, S. (2010). Observations of S410p and S350p phases at seismograph stations in California. *Journal of Geophysical Research*, *115*, B05303. https://doi.org/10.1029/2009JB006582

Vinnik, L. P., Foulger, G. R., & Du, Z. (2005). Seismic boundaries in the mantle beneath Iceland: A new constraint on temperature. *Geophysical Journal International*, *160*, 533–538. https://doi.org/10.1111/j.1365-246X.2005.02529.x

Vinnik, L. P. (1977). Detection of waves converted from P to SV in the mantle. *Physics of the Earth and Planetary Interiors*, *15*(1), 39–45. https://doi.org/10.1016/0031-9201(77)90008-5

Watt, J. P., Davies, G. F., & O'Connell, R. J. (1976). The elastic properties of composite materials. *Reviews of Geophysics*, *14*(4), 541–563. https://doi.org/10.1029/RG014i004p00541

Weidner, D. J., & Wang, Y. (1998). Chemical- and Clapeyron-induced buoyancy at the 660 km discontinuity. *Journal of Geophysical Research*, *103*(B4), 7431–7441. https://doi.org/10.1029/97JB03511

Whitmeyer, S. J., & Karlstrom, K. E. (2007). Tectonic model for the Proterozoic growth of North America. *Geosphere*, *3*, 220–259. https://doi.org/10.1029/2012JB009639

Williams, H., Hoffman, P. F., Lewry, J. F., Monger, J. W. H., & Rivers, T. (1991). Anatomy of North America: Thematic geologic portrayals of the continent. *Tectonophysics*, *187*(1–3), 117–134. https://doi.org/10.1016/0040-1951(91)90416-P

Wilson, D. C., Angus, D. A., Ni, J. F., & Grand, S. P. (2006). Constraints on the interpretation of S-to-P receiver functions. *Geophysical Journal International*, *165*, 969–980. https://doi.org/10.1111/j.1365-246X.2006.02981.x

Wölbern, I., Rümpker, G., Link, K., & Sodoudi, F. (2012). Melt infiltration of the lower lithosphere beneath the Tanzania craton and the Albertine rift inferred from S receiver functions. *Geochemistry, Geophysics, Geosystems*, *13*, 1–20. https://doi.org/10.1029/2012GC004167

Wood, B. J., & Holloway, J. R. (1984). A thermodynamic model for subsolidus equilibria in the system CaO MgO Al_2O_3 SiO_2. *Geochimica et Cosmochimica Acta*, *48*(1), 159–176. https://doi.org/10.1016/0016-7037(84)90358-2

Xiao, J., Hier-Majumder, S., Tauzin, B., & Waltham, D. (2020). An inversion approach for analysing the physical properties of a seismic low-velocity layer in the upper mantle. *Physics of the Earth and Planetary Interiors*, *304*, 106502. https://doi.org/10.1016/j.pepi.2020.106502

Xu, W., Lithgow-Bertelloni, C., Stixrude, L., & Ritsema, J. (2008). The effect of bulk composition and temperature on mantle seismic structure. *Earth and Planetary Science Letters*, *275*, 70–79. https://doi.org/10.1016/j.epsl.2008.08.012

Yuan, H., French, S., Cupillard, P., & Romanowicz, B. (2014). Lithospheric expression of geological units in central and eastern North America from full waveform tomography. *Earth and Planetary Science Letters*, *402*, 176–186. https://doi.org/10.1016/j.epsl.2013.11.057

Yuan, H., & Romanovicz, B. (2010). Lithospheric layering in the North American craton. *Nature*, *466*(7310), 1063–1068. https://doi.org/10.1038/nature09332

Yuan, H., Romanowicz, B., Fischer, K. M., & Abt, D. (2011). 3-D shear wave radially and azimuthally anisotropic velocity model of the North American upper mantle. *Geophysical Journal International*, *184*(3), 1237–1260. https://doi.org/10.1111/j.1365-246X.2010.04901.x

Yuan, X., Kind, R., Li, X., & Wang, R. (2006). The S receiver functions: Synthetics and data example. *Geophysical Journal International*, *165*, 555–564. https://doi.org/10.1111/j.1365-246X.2006.02885.x

Zhang, Q., Sandvol, E., & Liu, M. (2009). Lithospheric velocity structure of the New Madrid Seismic Zone: A joint teleseismic and local P tomographic study. *Geophysical Research Letters*, *36*, L11305. https://doi.org/10.1029/2009GL037687